

A.I.F.A. - ITALIAN ASSOCIATION FOR FATIGUE IN AERONAUTICS
DEPARTMENT OF CIVIL AND INDUSTRIAL ENGINEERING - UNIVERSITY OF PISA

**Review of aeronautical fatigue investigations
carried out in Italy
during the period April 2023 - March 2025**

by
D. Fanteria

Department of Civil and Industrial Engineering
University of Pisa – Italy
daniele.fanteria@unipi.it

This document summarizes the principal research activities carried out in Italy about aeronautical fatigue in the period April 2023 – March 2025. The main topics covered are operational load analysis, fatigue and fracture mechanics of metals, fatigue and damage tolerance of composites, Structural Health Monitoring, NDI methods.

CONTENTS

1	INTRODUCTION	1
2	MEASUREMENT AND ANALYSIS OF OPERATIONAL LOADS	1
2.1	<i>AMX General Status (Leonardo Aircraft Division)</i>	<i>1</i>
2.2	<i>Life monitoring of the TORNADO fleet (Leonardo Aircraft Division)</i>	<i>1</i>
2.3	<i>EF Typhoon life monitoring-Fleet Status (Leonardo Aircraft Division)</i>	<i>1</i>
2.4	<i>M-346 In-Service Monitoring (Leonardo Aircraft Division)</i>	<i>2</i>
2.5	<i>C-27J In-Service Life Monitoring-Fleet Status (Leonardo Aircraft Division)</i>	<i>3</i>
2.6	<i>EUROFIGHTER–Monitoring Wing Tip Fatigue due to Buffet (Leonardo Aircraft Division)</i>	<i>3</i>
2.7	<i>An artificial intelligence (AI) algorithm to evaluate inspection intervals based on in-service flown spectrum. (Leonardo Aircraft Division)</i>	<i>4</i>
2.8	<i>Dynamic optimization of an Aircraft Maintenance Plan based on structural integrity and equipment conditions (Leonardo Aircraft Division)</i>	<i>5</i>
2.9	<i>Enhancement of Helicopter Usage Monitoring through Machine Learning (Leonardo Helicopter Division)</i>	<i>6</i>
3	FATIGUE AND DAMAGE TOLERANCE OF METALS	11
3.1	<i>Fatigue behaviour</i>	<i>11</i>
3.1.1	<i>Interference Fit Fasteners with Cold working: improvement on Fatigue life evaluation (Leonardo Aircraft Division)</i>	<i>11</i>
3.1.2	<i>Additive Manufacturing Test Campaign-Titanium (Leonardo Aircraft Division)</i>	<i>11</i>
3.1.3	<i>Fatigue assessment of LSP treated joints: the «Pressure Floor» specimen (Univ. of Pisa)</i>	<i>13</i>
3.2	<i>Crack propagation and fracture mechanics</i>	<i>15</i>
3.2.1	<i>Fatigue crack propagation of 3-D defects from holes (Univ. of Pisa)</i>	<i>15</i>
3.3	<i>Corrosion</i>	<i>17</i>
3.3.1	<i>REACH–Test Campaign-Chemical Conversion (Leonardo Aircraft Division)</i>	<i>17</i>
3.3.2	<i>Corrosion Monitoring: a possible solution (Leonardo Helicopter Division)</i>	<i>18</i>
4	FATIGUE AND DAMAGE TOLERANCE OF COMPOSITES	22
4.1	<i>Fatigue in Adhesively Bonded Joints (Univ. of Bologna)</i>	<i>22</i>
4.2	<i>Propagation of interface damage in adhesive joint and interlaminar layers in static and fatigue loading (Milan Polytech.)</i>	<i>23</i>
4.3	<i>Hygrothermal ageing and monitoring (Milan Polytech.)</i>	<i>25</i>
4.4	<i>Economic Impact Assessment of SHM Systems in Aeronautical Structure (Milan Polytech.)</i>	<i>27</i>
4.5	<i>CFRP Fracture Properties for Crash Application (Univ. of Bologna)</i>	<i>29</i>
4.6	<i>Interlaminar properties of Various Composite Materials (Univ. of Pisa)</i>	<i>32</i>

5	NDI METHODS	35
5.1	<i>Methodology for Detectable Crack Length determination (Leonardo Helicopter Division).....</i>	<i>35</i>
6	AIRCRAFT FATIGUE SUBSTANTIATION	38
6.1	<i>AW169 –Cross Tubes Fatigue Life Recalculation supported by HUMS data (Leonardo Helicopter Division). 38</i>	
6.2	<i>C-27J Fire Fighting Usage Preliminary Concept (Leonardo Aircraft Division).....</i>	<i>40</i>
6.3	<i>TORNADO: Technical Evaluation-Fatigue and DT Analysis (Leonardo Aircraft Division).....</i>	<i>42</i>
6.4	<i>EUROFIGHTER Production Major Airframe Fatigue Test (Leonardo Aircraft Division).....</i>	<i>44</i>
6.5	<i>M345 Fatigue test on component status (Leonardo Aircraft Division).....</i>	<i>44</i>
6.6	<i>GCAP–Global Combat Air Programme (Leonardo Aircraft Division).....</i>	<i>45</i>
7	REFERENCES	46

1 INTRODUCTION

This paper summarises aeronautical fatigue investigations carried out in Italy during the period April 2023 to March 2025. The different contributions have been arranged according to the topics, which are operational load analysis, fatigue and damage tolerance of metallic materials, fatigue and damage tolerance behaviour of composites, NDI methods AND aircraft fatigue substantiation.

The review is based on the activities carried out within the various organisations belonging to A.I.F.A., the Italian Association for Fatigue in Aeronautics. The author gratefully acknowledges the fundamental contribution, which has made this review possible, given by several A.I.F.A. members, who are the representatives of Universities and Industries in A.I.F.A.

2 MEASUREMENT AND ANALYSIS OF OPERATIONAL LOADS

2.1 AMX General Status (Leonardo Aircraft Division)

On 5 April 2024, the Italian Air Force formally concluded its AMX fleet with a ceremony held at the Istrana air base, home of the 132° Squadron, the final unit to operate the light bomber and reconnaissance aircraft. This was the final act for the AMX.

The AMX aircraft was developed by the Italian/Brazilian consortium (46.5% Alenia, 22.8% Aermacchi and 29.7% Embraer), and has been in active service for over thirty years in Italy (10 single-seat and 26 twin-seat) and in Brazil (56 single-seat).

2.2 Life monitoring of the TORNADO fleet (Leonardo Aircraft Division)

Italy is participating in the Panavia Tornado aircraft programme through Leonardo, which is operating in partnership with BAE Systems in the UK and Airbus Defence and Space in Germany. The Italian Air Force is currently operating 37 of the 99 Tornado aircraft that were delivered between May 1982 and July 1989.

Throughout the operational life of the Italian Tornado Fleet, Leonardo has been performing life monitoring (totalling approximately 300,000 flight hours analysed) until the end of 2016, when the Maintenance Recorder System (Ma.Re.S) was put into service. Since 2017, Leonardo has been contracted for the resolution of issues pertaining to Ma.Re.S malfunctions and the provision of database updates, consequent to the life extension of specific aircraft components.

At present, Leonardo is participating in the life extension programme for the German fleet, with a target of 8,000 flight hours.

2.3 EF Typhoon life monitoring-Fleet Status (Leonardo Aircraft Division)

The Italian Air Force fleet of EF Typhoons is composed by 95 airplanes, 81 Single Seater (SS) and 14 Twin Seater (TS), in service since 2003. The fleet has accumulated about 176000 Flight Hours FH, corresponding to about 11500 flights.

A Structural Health Monitoring (SHM) system is installed on each aircraft and allows individual aircraft in-service monitoring. The SHM monitors ten significant locations on the structure to derive the flown spectrum in terms of aircraft load factor (N_z) and to evaluate the Usage Factor at the monitored locations. The Usage Factor is defined as the ratio between the mean hourly life consumption and the design one: $(\text{Usage factor}) = (\text{in-service usage rate}) / (\text{design usage rate})$.

In terms of N_z Spectrum both SS and TS fleets are flying within the design envelope. The Usage Factor rate is below the design value for all the 10 locations for both variants as shown in Figure 2.1.

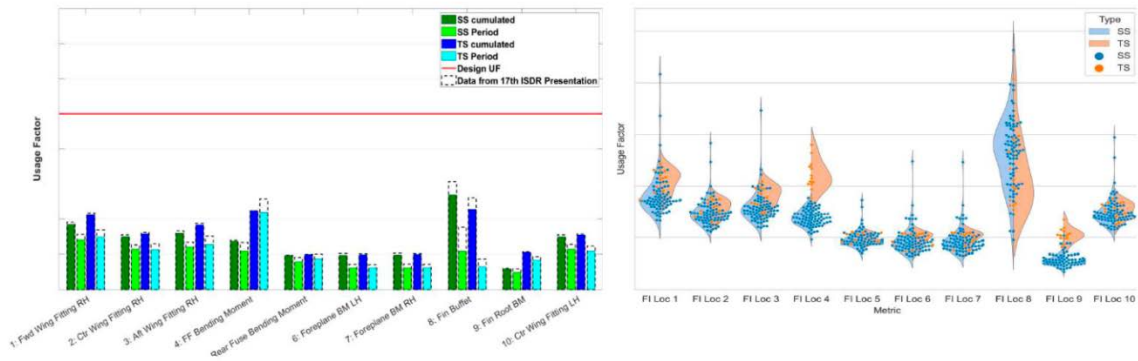


Figure 2.1 Usage Factor for the 10 monitored locations.

In addition, a specific damage spectrum is derived for stress due to vibrations induced in flight conditions in which the airbrake is used. An example of the Airbrake Out Damage Spectrum is shown in Figure 2.2

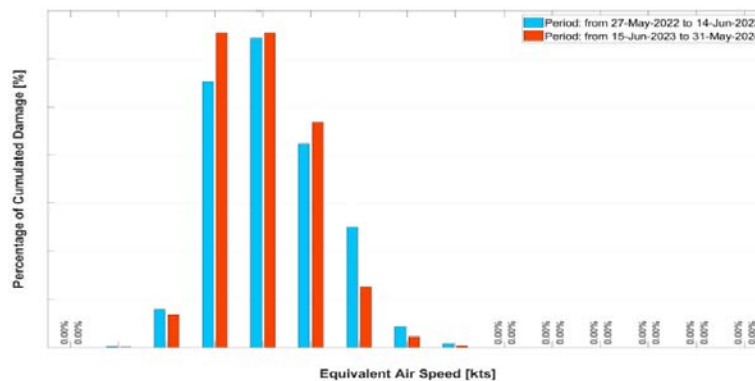


Figure 2.2 Airbrake Out Damage Spectrum example for the IAF Typhoon fleet.

2.4 M-346 In-Service Monitoring (Leonardo Aircraft Division)

The M-346 has been selected by several countries to serve as an advanced trainer for their pilots; 85 aircraft are currently in service, with major customers including the Italian Air Force (ItAF) with 22 aircraft, including 4 aircraft operated by the International Flight Training School (IFTS), the Israeli Air Force (IAF) with 30 aircraft, and the Republic of Singapore Air Force (RSAF) with 12 aircraft.

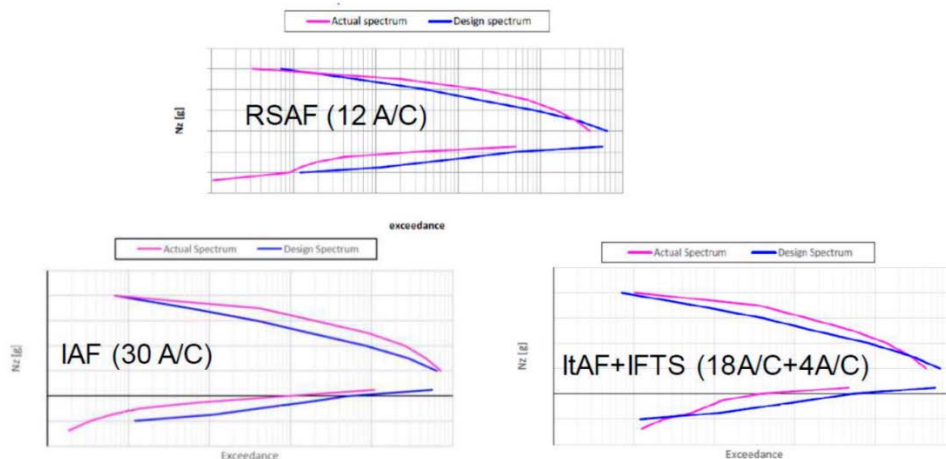


Figure 2.3 Non-dimensional Real N_z spectrum of different M-346 fleets.

M-346 Advanced Trainer implements a Health & Usage Monitoring System (HUMS) that enables monitoring both on-board equipment and structure. Data analysis, based on a non-parametric statistic, allows actual aircraft spectra usage being evaluated; examples are shown in Figure 2.3 for three of the major fleets.

2.5 C-27J In-Service Life Monitoring-Fleet Status (Leonardo Aircraft Division)

The Italian Air Force has an active fleet of C-27J composed of 12 aircraft and at the latest available update (April 2024) a total of about 38300 flights had been monitored for almost 54000 flight hours, overall.

The monitoring is performed through a specifically developed Individual Aircraft Tracking Program (I.A.T.P.) software, that runs on ground; the software monitors the fatigue life of each aircraft based on the actual mission profiles and load spectra determined by means of the direct recording of in-flight parameters.

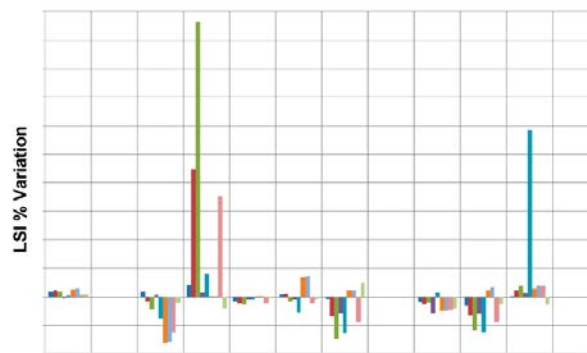


Figure 2.4 LSI percentage variation at monitored locations over the last period.

The I.A.T.P. software monitors the main representative locations of structural items through the calculation of the Load Severity Index (LSI), which is the ratio between the In-Service Life Damage and the Design Life Damage. The Design Life Damage is the fatigue damage calculated under theoretical mission profiles and mixing, which were applied during the full-scale fatigue testing. In conclusion, the LSI measures the different severity among in-service and design usage.

Figure 2.4 shows the trend of LSI variations in the last period of observation: the fleet fatigue behaviour for the period is very close to previous one, within a variation of $\pm 2,5\%$, except for aircraft affected by relevant manoeuvre loads. The fleet typically performs flights of a duration shorter than design and at a higher altitude than design mission profiles.

2.6 EUROFIGHTER–Monitoring Wing Tip Fatigue due to Buffet (Leonardo Aircraft Division)

The system employs a parametric approach to estimate structural stress, enabling the detection of the onset of buffet and the prediction of potential fatigue damage without the need for direct strain measurements. The main procedure is outlined in three steps:

1. *Flight Envelope definition.* Key flight parameters (such as equivalent airspeed, altitude and angle of attack) are analysed to establish boundaries within which the aircraft is susceptible to developing fatigue issues due to buffeting.

2. *Detection of Buffet within Flight Envelope.* The Buffet Normalized Level (BNL) filter is used to identify flight conditions where aerodynamic buffet occurs, allowing load contributions caused by the buffet to be identified using a predictive model.

3. *Structural damage assessment during the buffet phenomenon.* Detailed time histories of A/C parameters during the buffet phenomena are sent to the loads department. The loads department

then produces a stress history, which is used to calculate fatigue consumption. To enhance the accuracy of the damage assessment, an algorithm based on a linear regression model is also applied.

This procedure allows the monitoring at the wing tip to be validated by comparing the results with strain gauge data from other aircraft systems.

2.7 An artificial intelligence (AI) algorithm to evaluate inspection intervals based on in-service flown spectrum. (Leonardo Aircraft Division)

A software solution has been developed that utilises a recurrent neural network (RNN) to calculate inspection intervals directly from in-flight recorded load histories. This innovative approach effectively bypasses the NASGRO crack propagation analysis process, as illustrated in Figure 2.5.

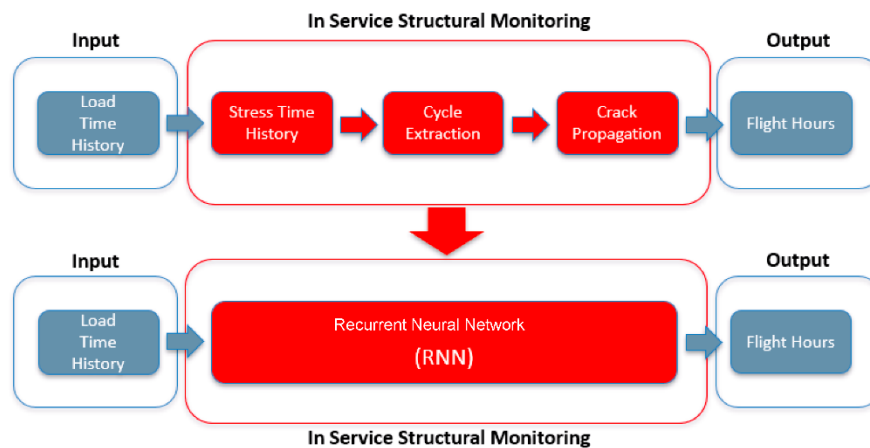


Figure 2.5 Recurrent neural network (RNN) algorithm to evaluate inspection intervals based on in-service flown spectrum.

Once trained on a relevant test case (A/C wing root section), the RNN model, compared to the traditional analysis approach, delivers the following results (see Figure 2.6):

- Accurate prediction of inspection interval for the average and most typical values.
- Conservative prediction for the highest values.
- Non conservative prediction for the lowest values.

The results have been computed in just 1 second, as opposed to the 15 minutes required by traditional analysis. This represents a substantial gain in terms of computational time.

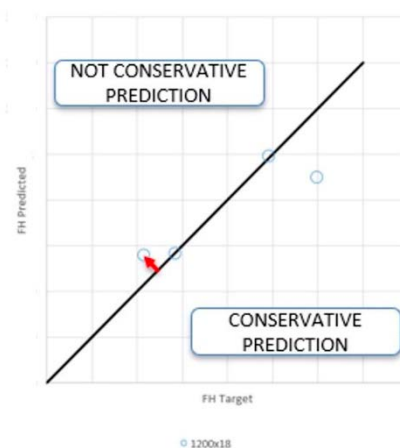


Figure 2.6 Recurrent neural network (RNN) algorithm: test case results.

Following this preliminary trial, the advantages and disadvantages of the AI (Artificial Intelligence) algorithm are outlined in Table 2.1.

Pros	Cons
The time required to evaluate an inspection interval has decreased considerably.	A significant amount of time is required to train the RNN (109 hours were spent learning from 18,432 load histories for the test case).
Operators will have the option to re-evaluate inspection intervals in real time, thereby adapting inspection plans with minimal support from an OEM specialist.	To manage large volumes of data, it is essential to have significant amounts of CPU power and memory capacity.

Table 2.1 Pros and Cons of the recurrent neural network (RNN) algorithm.

Following the encouraging results of the preliminary trial, the next development points are as follows:

- The training strategy for the test case is to be improved, with the number of training samples increased and data augmentation refined.
- For the same test case, it is essential to enhance the RNN prediction capability, ensuring that the results are always conservative.
- The lesson learned from the simple test case should be used to define the RNN for a more complex model (i.e. a model that is subject to more than one load component, etc.).

2.8 Dynamic optimization of an Aircraft Maintenance Plan based on structural integrity and equipment conditions (Leonardo Aircraft Division)

A thesis has been developed at the University of Rome 'La Sapienza' that focuses on optimising the maintenance plan (MP) for a multi-purpose transport aircraft. Currently, the MP outlines all scheduled maintenance actions and how frequently they should be completed.

The aim was to introduce new adaptive strategies to create a dynamic structural maintenance plan based on fleet data. The main objectives were:

- Definition of dynamic maintenance tasks using in-service data
- Tailoring tasks to specific tail numbers.
- Evaluation of direct effects on scheduled inspections
- Assessment of operational and economic benefits.

To represent the aircraft's overall operational severity spectrum, in terms of both fatigue and crack propagation, a mean load severity index has been calculated:

$$LSI_{\text{mean}} = (LSI_{\text{fatigue}} + LSI_{\text{prop.}})/2.$$

As a ratio, the LSI indicates whether the global operational severity is higher or lower than the design hypothesis.

The general idea behind the proposed approaches is sketched in Figure 2.7.

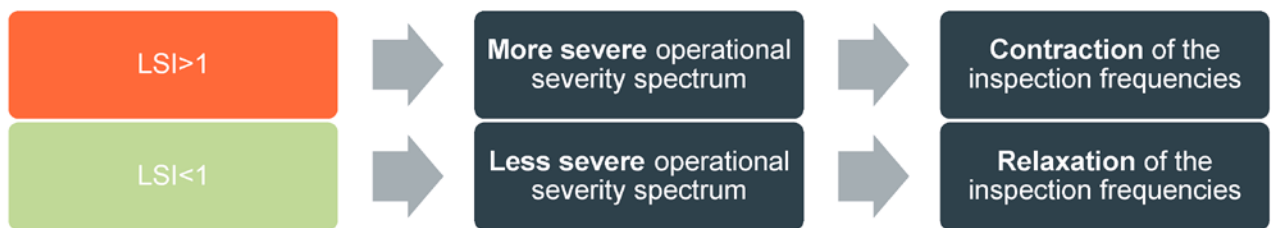


Figure 2.7 The general idea behind the proposed dynamic approaches

Two models have been developed for a dynamic maintenance planning approach:

- Model 1. This model modifies the prescribed threshold and intervals, dividing them by the relative LSI. It is similar to the logics of severity-based aircraft usage. The main issue is the significant impact on current inspection times when the LSI deviates substantially from its unitary value.
- Model 2. The purpose of this model is to solve the significant modifications imposed by the dynamic LSI-based model by instructing a modification function based on the mean Load Severity Index. The dynamic nature is limited to a defined percentage of the inspection time under consideration. A fixed percentage of the inspection time does not vary. The remaining part (the variable percentage) can contract or expand according to the LSI value.

2.9 Enhancement of Helicopter Usage Monitoring through Machine Learning (Leonardo Helicopter Division)

Helicopter maintenance plans are normally defined on the basis of expected (design) mission profiles, that may be quite different with respect to the actual scenario in which the helicopters will operate. The definition of an improved maintenance plan can be achieved through a periodical validation of the initial usage hypothesis, that can confirm or suggest proper amendments so to develop diversified Maintenance Plans tailored to the actual usage of every specific fleet (the so-called Effective Maintenance Plans).

Benefits expected by such an approach are the evolution from Time-Based Maintenance (TBM) to Condition-Based Maintenance (CBM), a reduction of Maintenance Costs which are a substantial portion ($\approx 25\%$) of Direct Operating Costs, and an increase of Flight Safety.

An Effective Structural Usage Monitoring (ESUM) is possible only if an effective and reliable Flight Condition Recognition (FCR) is available. An essential requirement for such a system is the capability to analyse automatically and swiftly large data sets registered by a fleet of 'Family' helicopters.

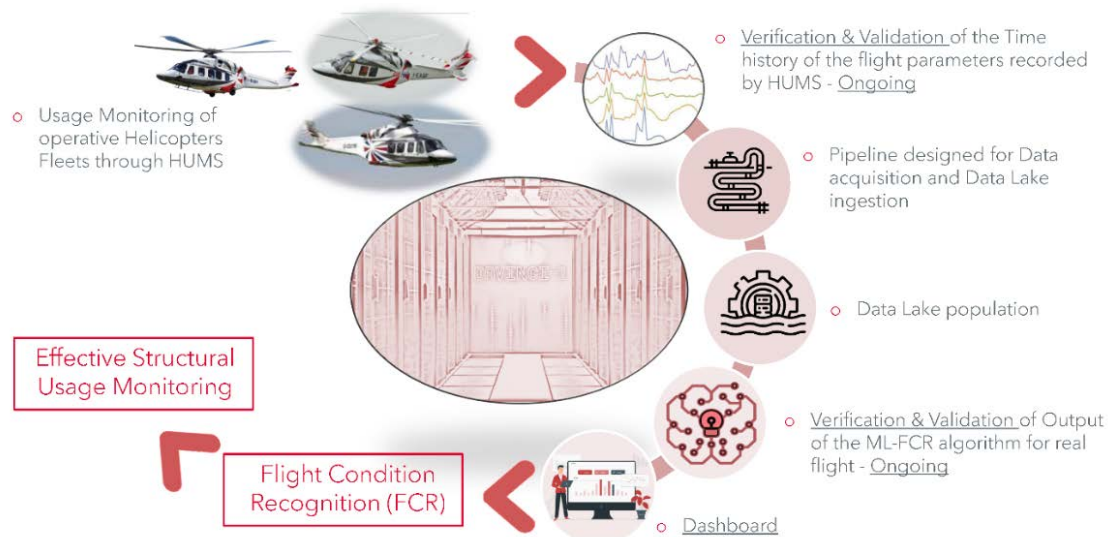


Figure 2.8 General Logic of the Flight Conditions Recognition analysis software.

A research programme was developed, in cooperation with two Departments of Milan Polytechnic (Department of Mechanical Engineering and Department of Electronics, Information and Bioengineering), with the purpose of developing an advanced software tool, capable to provide an

automatic, reliable, and efficient analysis of the time histories of the principal usage parameters recorded on board during flight operations. Previous edition of this National Review already described the first results of this joint effort.

AW189		AW169		AW139	
					
Number of maneuvers	> 5100	Number of maneuvers	> 5200	Number of maneuvers	> 8000
Number of flights	> 230	Number of flights	> 220	Number of flights	≈ 600

Table 2.2 AW – Family Products data sets used for developing the ML Algorithm.

A Flight Conditions Recognition (FCR) algorithm was developed adopting a combination of Machine Learning (M/L) approaches, which are particularly suitable for the analysis of massive data set structures (Big-Data). The logic of the approach to Flight Conditions Recognition is explained in Figure 2.8. The data “lake” is composed of the time sequences of the principal flight parameters recorded by the HUMS fitted on board.

To develop the ML Algorithm a specific Dataset of Load Survey Flights composed by Labelled Manoeuvres was used (see Table 2.2 for info about number of flights and manoeuvres employed). Three fourths of the dataset have been used for Training the Supervised ML Algorithm while the remaining flights and manoeuvres have been devoted to Testing & Verifying.

The major challenge of the activity is related to manoeuvre recognition, because of the inherent differences in duration and loading factor that can be ascribed to piloting techniques and to the environment. An additional issue related to manoeuvres is their combination, which may occur in practice when two manoeuvres are executed contemporarily.

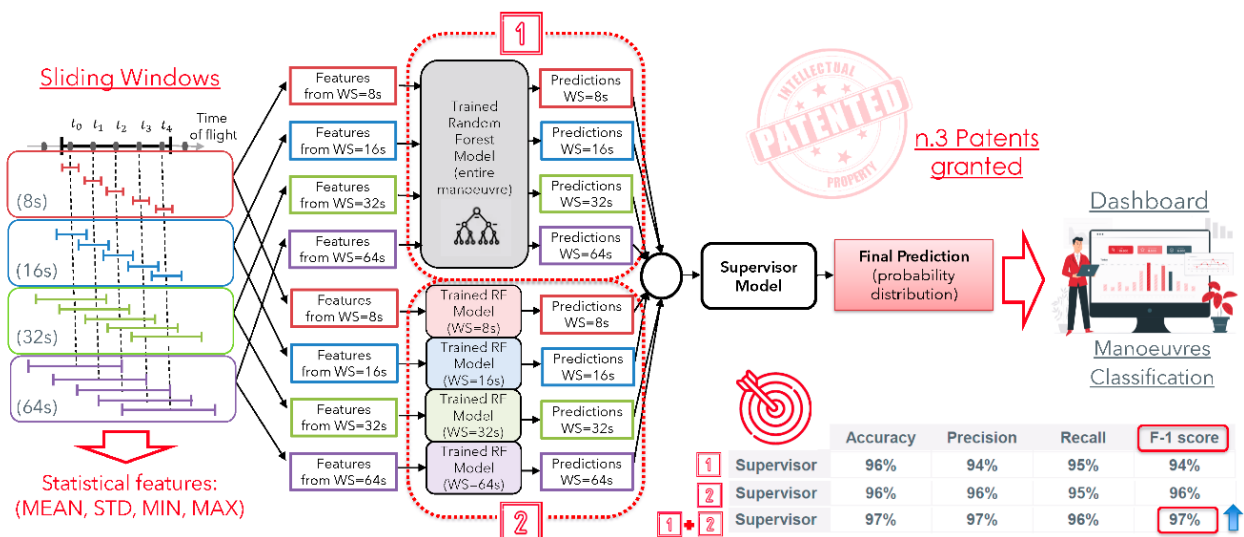


Figure 2.9 Machine Learning (M/L) Algorithm

A rebalancing procedure of the dataset was developed to improve the performance of the Machine Learning (ML) algorithm. Dataset rebalancing is organised in two steps: a first step that aggregates manoeuvres with similar characteristics into Macro-categories and a second step that identifies single Flight Conditions inside the macro-categories via deterministic features.

Since the data set for training the system cannot cover all combinations, statistical features are extracted analysing the time histories by means of “sliding windows” and two strategies employed to elaborate predictions; finally, a supervisor algorithm chooses the best option (Figure 2.9).







AW189 	 (HUMS Family)	PREDICTION ACCURACY ON PARTITIONED MANEUVERS 98.5%	PREDICTION ACCURACY ON <u>FULL FLIGHTS at 1st Classification Level</u> 97.3%
AW139 	 (HUMS LH)	PREDICTION ACCURACY ON PARTITIONED MANEUVERS 96.8%	PREDICTION ACCURACY ON <u>FULL FLIGHTS at 1st Classification Level</u> 96.4%
AW169 	 (HUMS Family)	PREDICTION ACCURACY ON PARTITIONED MANEUVERS 98.5%	PREDICTION ACCURACY ON <u>FULL FLIGHTS at 1st Classification Level</u> 97.3%

Figure 2.10 Machine Learning (M/L) Algorithm: performance for Load Survey flights.

The Algorithm has been further tested and Figure 2.10 shows an example of the performance obtained on the presented test case.

The Dashboard (see Figure 2.8) permits to visualize the results of the M/L Algorithm. This aspect has been further enhanced in the period covered by this review to include 3 Environments: The Flight Explorer the Helicopter Explorer and the Fleet Explorer (Figure 2.11). They allow visualizing the results in terms of classified manoeuvres both in a Detailed and an Aggregated way.



Figure 2.11 Dashboard – Front End interface.

The Flight Explorer environment offers detailed Information at Flight Level such as visualize a single flight and explore how it was segmented in terms of recognised manoeuvres, access to the individual recognised manoeuvre to verify the trends of the characteristics flight parameters or Visualize durations and occurrences of the recognised flight regimes. An example of the data available in such environment is shown in Figure 2.12.



Figure 2.12 Flight Explorer environment – example of a mission with recognised manoeuvres.

The Helicopter Explorer environment shows aggregated information such as how a specific helicopter has been used across several different flights, the amount of time spent in every recognised manoeuvre by a specific helicopter of the fleet, or the number of occurrences of any recognised flight regimes for a particular helicopter. An example of the data available in such environment is shown in Figure 2.13.

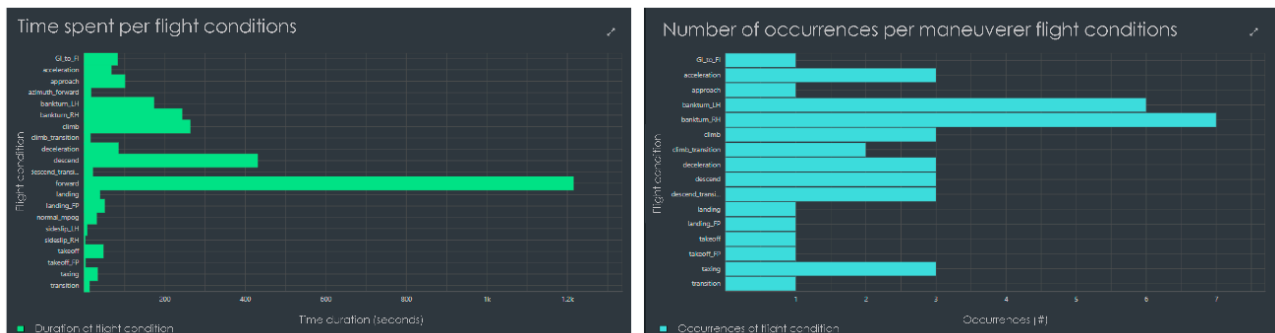


Figure 2.13 Helicopter Explorer environment: aggregated data example.

The Fleet Explorer environment shows aggregated information such as how fleet has been used across several different flights, the total time spent by the considered fleet in each recognised manoeuvres, or the duration and occurrences of the recognised flight regimes. An example of the data available in such environment is shown in Figure 2.14.

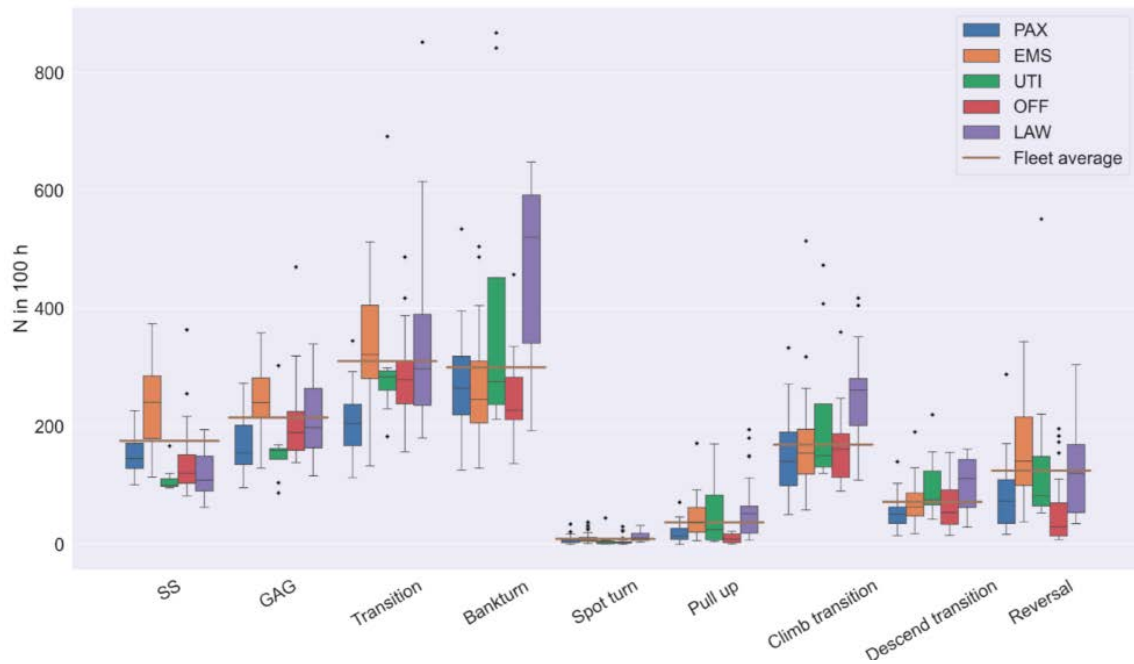


Figure 2.14 Fleet Explorer environment: aggregated data example.

The proposed Multi-Strategy ML-based approach has been demonstrated to be robust, Flexible (easily adaptable to different aircraft variants), Scalable and it is inherently re-trainable if more or different measurements are available.

3 FATIGUE AND DAMAGE TOLERANCE OF METALS

3.1 Fatigue behaviour

3.1.1 Interference Fit Fasteners with Cold working: improvement on Fatigue life evaluation (Leonardo Aircraft Division)

A research programme has been initiated to evaluate the combined effects of cold working (CW) and interference fit (IF) installation on the fatigue performance of joints using OSI bolts.

Various joint configurations and different load transfer rates (i.e. the bearing load divided by the total load) are being considered.

A theoretical analysis has been performed to define a preliminary factor that takes into account the combined effect of CW and IF in the fatigue analysis of joints.

This analysis is based on assumptions and data reported in AGARD R-721 ('Fatigue Rated Fastener Systems') and the ESDU series 'Fatigue of Aluminium Alloy Joints with Various Fastener Systems' for different load transfer levels: Low Load Transfer (ESDU 89046), Medium Load Transfer (ESDU 90009), and High Load Transfer (ESDU 90018).

A dedicated test campaign on specific coupons is in progress to substantiate and refine such a factor. The test matrix comprises approximately 100 specimens (parts made of Al7050-T7451) using different types of fastener. Tests are being conducted with constant amplitude (varying maximum load) and variable amplitude loading (FALSTAFF spectrum).

3.1.2 Additive Manufacturing Test Campaign-Titanium (Leonardo Aircraft Division)

A test campaign was developed to estimate the fatigue and crack propagation behaviour of Ti-6Al-4V specimens fabricated using Additive Manufacturing based on Powder Bed Fusion Technology.

This study, conducted on approximately 200 specimens, aimed to evaluate the impact of various structural and geometric features (e.g. open holes, notches, and joints) and process parameters (e.g. roughness and fabrication direction) on fatigue properties.

The specimens were fabricated from Grade 23 titanium powder from different batches, using different stratification strategies. The three batches of powder differ in the amount of recycled powder used: batch 1 contains 50% recycled powder; batch 2 contains 66%; and batch 3 contains 81%. Virgin powder completes the volume to 100%.

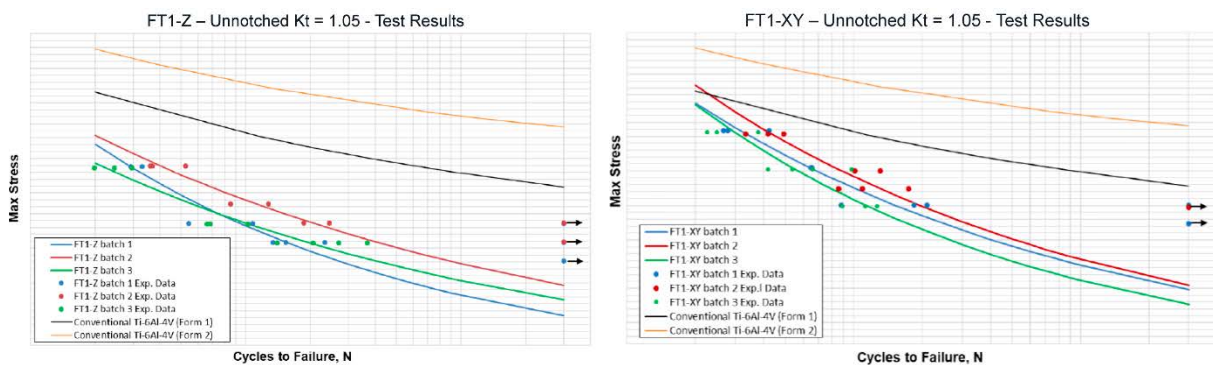


Figure 3.1 Fatigue tests results on unnotched specimens, different deposition directions.

The following tests have been conducted: Fatigue tests (S/N curve determination), fatigue crack growth and fracture toughness.

Fatigue testing (EN 6072, S/N curves) has been performed on four types of specimen: unnotched ($K_t = 1.05$), notched ($K_t = 3.0$), lugs, and joints. The tests were carried out at room temperature and ambient conditions, with loading cycles at a constant amplitude of $R = 0.1$ and a frequency of at

least 10 Hz. In-plane stratification (direction XY) and vertical stratification (direction Z) were used to fabricate different batches for the same test type.

Crack growth rates as a function of the stress intensity factor K were derived at $R = 0.1$ in accordance with the ASTM E647, and fracture toughness was evaluated in accordance with the ASTM E399 standard.

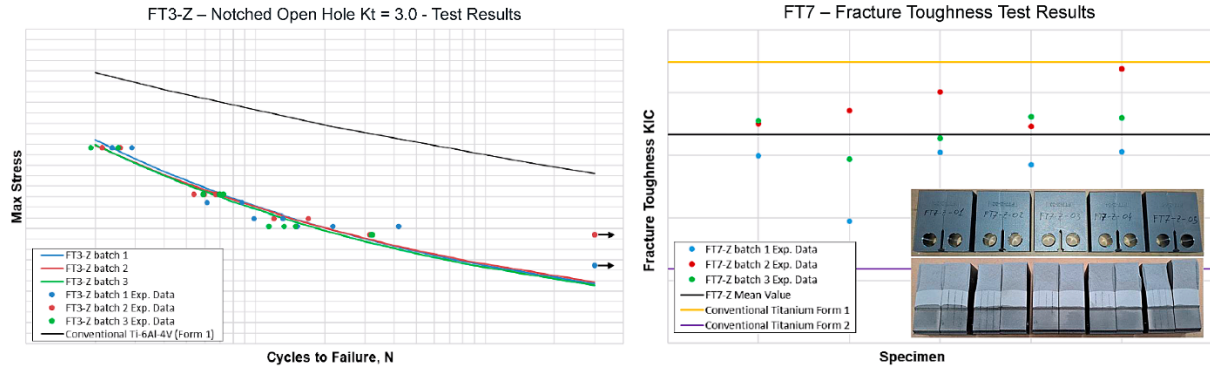


Figure 3.2 Fatigue tests results on notched specimens and fracture toughness test results.

The results of the fatigue tests on unnotched specimens fabricated with different deposition directions are shown Figure 3.1. Two S-N curves for conventional titanium (Ti-6Al-4V, not additive manufactured) are shown for reference (two forms obtained from the literature).

The results of fatigue tests on notched specimens are shown in Figure 3.2 on the left. An S-N curve for conventional titanium (Ti-6Al-4V, not additive manufactured) is shown for reference.

Fracture toughness test results are shown in Figure 3.2 on the right, alongside relevant reference data for the conventional Ti-6Al-4V titanium alloy (two forms). Batch-to-batch variability is small.

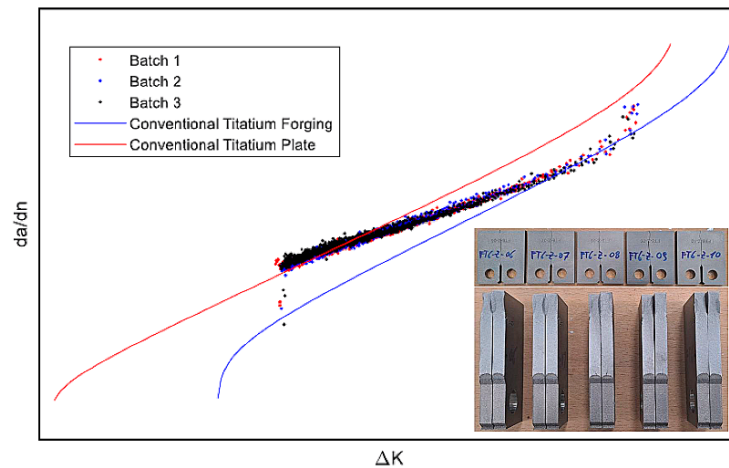


Figure 3.3 Crack propagation tests results.

Figure 3.3 shows the results of the crack propagation tests for the three batches. As in the previous case, two reference curves are added for conventional titanium plates and forgings. There is low batch-to-batch dispersion, and the AM data are between the reference curves (the AM propagation data have a smaller slope in the Paris region).

In conclusion, specimens obtained by means of additive manufacturing show high surface roughness. Specimens fabricated with an XY stratification direction exhibit better fatigue behaviour than specimens obtained with a Z stratification direction. The percentage of recycled powders does not clearly influence fatigue behaviour; therefore, for fatigue evaluation purposes, it is possible to consider a single S-N curve obtained by averaging across batches.

Fatigue crack growth test results show a comparable crack growth rate for AM specimens to that of a conventional Ti-6Al-4V alloy, with AM data between the forged and plate forms.

3.1.3 Fatigue assessment of LSP treated joints: the «Pressure Floor» specimen (Univ. of Pisa)

An experimental activity was carried out at the University of Pisa in collaboration with Airbus Operations GmbH to study the fatigue behaviour of a joint with holes that were treated using different processes intended to enhance the fatigue resistance of the item.

The “pressure floor” specimen, shown in Figure 3.4, is quite simple with only two elements: the “dog bone” (inspired by a detail of the floor of the centre fuselage of a narrow-body aircraft, hence the name) and an L-shaped angle bracket (corner fitting), connected to the dog bone by three fasteners.

The specific objective of the activity was to assess the efficiency of Laser Shock Peening in enhancing the fatigue life of the specimen in comparison with a more traditional process such as Cold Expansion. The specimens were LSP-treated by AB, but the assembly operations, including cold expansion where necessary, were performed in Pisa. The fatigue test campaign was carried out using constant amplitude loading with a stress ratio of $R = 0.1$.

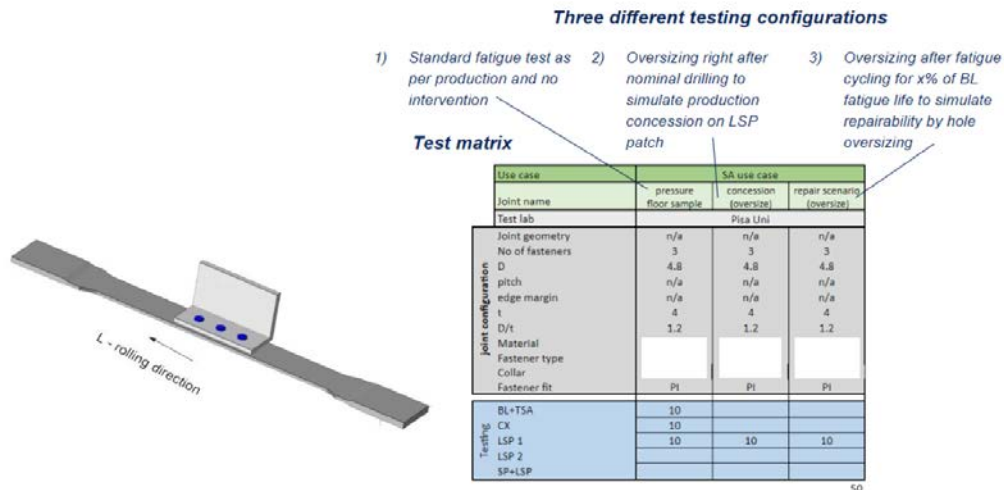


Figure 3.4 The «Pressure Floor» specimen and the test matrix.

As shown in the Test Matrix table (see Figure 3.4), there were three different specimen configurations, each one described in a column: the basic configuration, the concession scenario and the repair scenario. These configurations require three types of fastener because the diameter changes. The fasteners have been installed with a production interference (PI) fit, which has been interpreted as an interference in the range of 30–60 microns.

The repair scenario specimens were not tested, but two LSP solutions were developed. Therefore, different diameter reamers have been used to prepare the holes for the “basic” and “concession” fasteners: 4.75 mm and 5.46 mm respectively.

The fasteners could not simply be inserted by hand, so a special tool was developed for use with a servohydraulic fatigue machine to install them. To increase the similarity with reality, the sealant was also applied. Four groups of “basic” configuration specimens were assembled: the baseline, Cx, LSP1 and LSP2. The “concession” scenario specimens were prepared with LSP1 dog-bones.

Before starting the fatigue testing, it was considered appropriate to study the strain distribution on the specimen. Four pairs of strain gauges have been bonded back-to-back on the dog-bone element to also assess the bending in these sections. The strain gauges are HBK LY13-1.5/120. To provide direct access to the dog-bone surface, two recesses were milled into the “corner fitting”. This operation has been deemed to have negligible consequences for the stress distribution. A sketch showing the position and numbering of the strain gauges is provided in Figure 3.5.

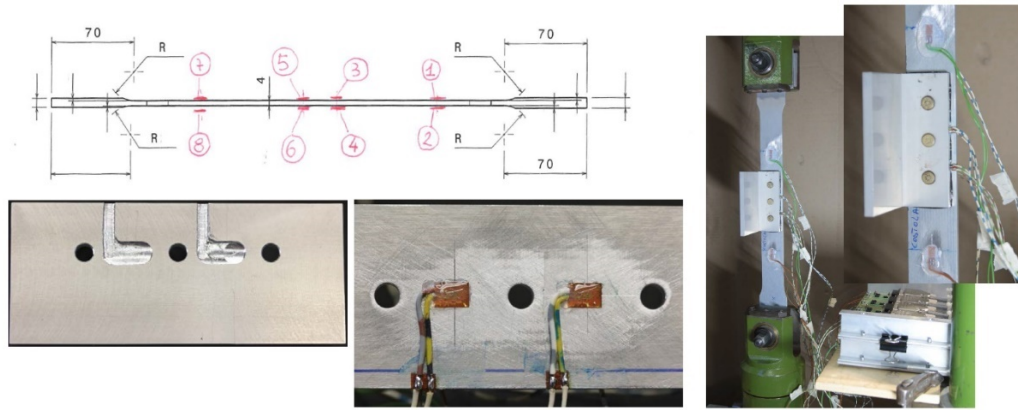


Figure 3.5 Development of the instrumented specimen to determine grip shims.

Following a number of trials, the optimal positioning of the instrumented specimen relative to the machine grips was determined using appropriate shims. The centre of gravity (C.G.) of the central joint was aligned with the actuator centre line. A bolt, tightened with a prescribed torque, applies a force to the specimen's faces, introducing the load by friction (see Figure 3.5).

The results of the static tests in terms of secondary bending at the strain gauge location were in satisfactory agreement with the numerical results obtained using an FE model (the measured values are given in Table 3.1).

1-2	3-4	5-6	7-8	Sg couples
1977.1	1490.2	1572.4	1995.8	Average
0.398	12.058	8.829	-4.834	S.B. (%)

Table 3.1 Stain gauge readings: average strains ($\mu\text{m/m}$) and secondary bending (%).

The first group of tests to be evaluated was the baseline group. Then, the LSP1 and Cx groups were tested. The results are shown in Figure 3.6. The LSP1 results were similar to the baseline results, but CX treatment ensured slightly better fatigue performance.

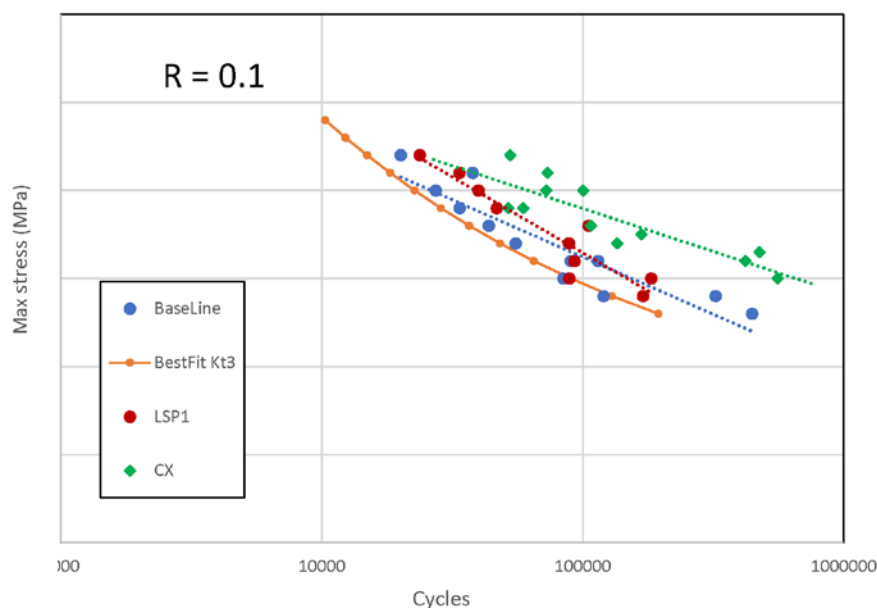


Figure 3.6 “Pressure floor” specimens fatigue results: LSP1, CX and baseline.

The final group to undergo testing was LSP2, for which a distinct set of parameters was employed for the LSP treatment.

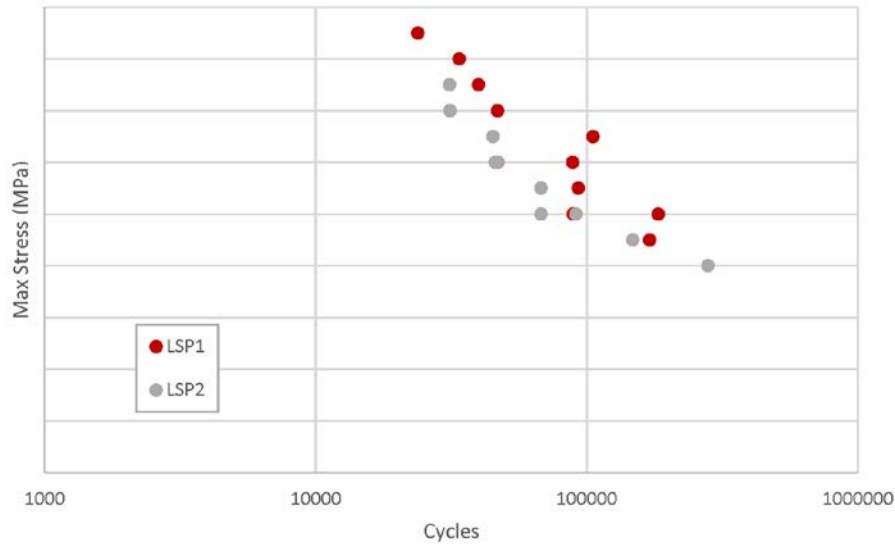


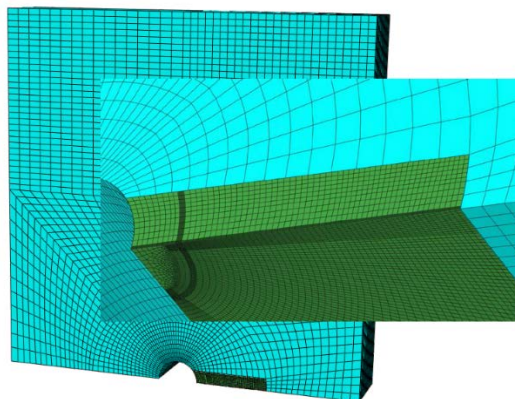
Figure 3.7 “Pressure floor” specimens fatigue results: LSP1 vs LSP2.

The LSP2 results are shown in Figure 3.7 alongside the LSP1 data. The new LSP setup did not improve the results, and the fatigue data for this second set of specimens are comparable with the baseline results.

3.2 Crack propagation and fracture mechanics

3.2.1 Fatigue crack propagation of 3-D defects from holes (Univ. of Pisa)

The Department of Civil and Industrial Engineering – Aerospace Section at the University of Pisa is conducting research into a comprehensive strategy for capturing fatigue crack growth in complex three-dimensional problems. Corner cracks have been considered, and two load cases examined: one corresponding to an open-hole specimen, and the other to a pin-loaded hole. Previous activities have generated experimental data using 2024-T351 specimens, which have been described in former editions of the National Review.



- Specimen partitioning in “hot” and “cold” zone
- Structured meshing technique
- Accurate partitioning near crack front
- J-Integral to calculate SIF

Figure 3.8 Corner Crack modeling approach for fatigue crack growth.

Numerical models have been developed using the commercial software ABAQUS 2022 in which the crack front is permitted to propagate freely and take on any shape. For this purpose, the initial crack front, which is defined as a quarter-ellipse, is updated using a spline curve during fatigue evolution. The values of the Stress Intensity Factor (SIF) are calculated along the previous front using the J-Integral technique, considering a given remote stress corresponding to the maximum cyclic stress in CA fatigue loading, and each subsequent front is determined based on these values.

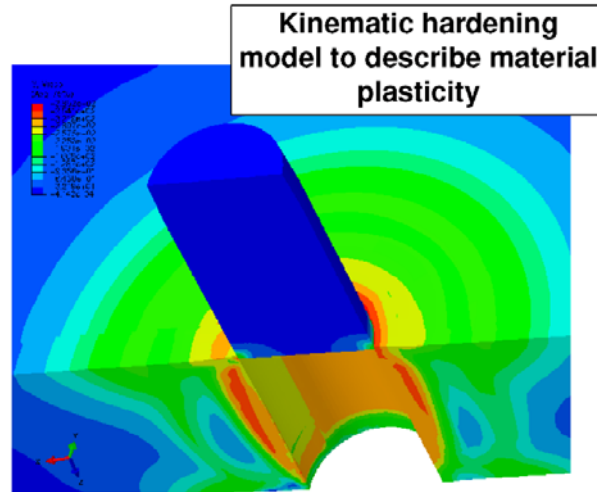


Figure 3.9 Stress field (von-mises) after non-linear simulation of cold expansion.

The SIF values are used to predict crack growth at 2,000-cycle intervals, in accordance with the propagation law defined by the NASGRO equation for the material.

The adopted modelling approach consists of dividing the specimen into two distinct parts: a small region containing the defect, which is discretised using a highly refined, structured, mesh (the “hot zone”); and a complementary region, which is meshed using a significantly coarser grid (the “cold zone”). These two parts are connected via a tie constraint to restore the component's structural integrity (see Figure 3.9). This approach enables a highly refined mesh to be created close to the crack front, with regular paths that facilitate convergence in J-integral calculations. This improves the accuracy of the SIF distribution along the front, even in regions close to free surfaces where there are high stress gradients in the elastic solution near the corner points.

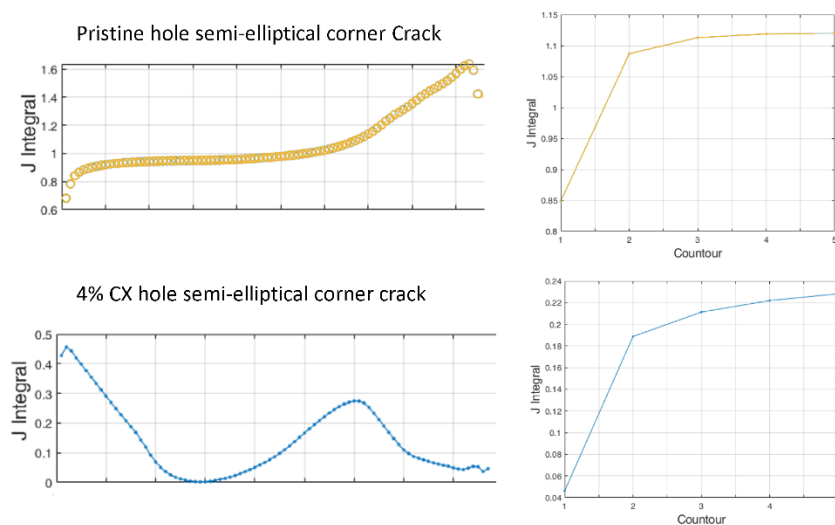


Figure 3.10 J-integral distribution along the crack for the two cases.

Then, compressive residual stresses resulting from a 4% cold expansion treatment were introduced using a nonlinear analysis that included kinematic hardening to model material plasticity. Material behaviour was modelled using a user subroutine. This enabled the same model to be used for non-linear elastoplastic analysis to evaluate the residual stress field induced by cold expansion, and subsequently for a linear analysis to evaluate the stress intensity factor via the corrected J-integral procedure. Figure 3.10 shows the stress field resulting from the simulation of cold expansion at the start of the linear analysis used to evaluate the J-integral distribution and the SIF.

The crack growth behaviour of the cold-expanded specimen was then compared with that of the untreated specimen, both undergoing a single load block of 2,000 cycles. The results are shown in Figure 3.12 in terms of J-integral distribution along the crack front. The same figure also illustrates the convergence rate of the J-integral calculation procedure.

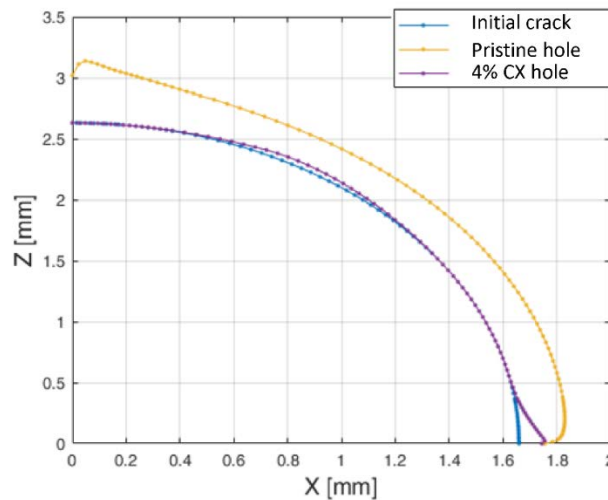


Figure 3.11 Crack propagation tests results.

Figure 3.13 shows the propagated crack fronts for the pristine condition and the CX expanded case, both from the same initial condition. According to the results, the residual stress field inhibited propagation for the first 2,000 cycles. These preliminary results are being verified in more complex conditions with an experimental counterpart, with the ultimate aim of validating the approach quantitatively.

3.3 Corrosion

3.3.1 REACH-Test Campaign-Chemical Conversion (Leonardo Aircraft Division)

In recent National Reviews, information was given about an experimental program, in progress at Leonardo Aircraft Division, for the assessment of the influence of protective treatments, compliant with the current international environmental regulation (**REACH** – **R**egistration, **E**valuation, **A**uthorization and **R**estriction of **C**hemicals), on the fatigue behaviour of the most common metallic alloys. Leonardo Aircraft Division has carried out several research activities with the aim of replacing different metal surface protection processes based on hexavalent chromium with more ecological ones, performed using trivalent chromium products.

To assess the impact of the new coating process on fatigue behaviour, a fatigue testing campaign was planned for aluminium alloys commonly used in Leonardo's proprietary programmes: an aluminium-copper alloy from series 2000 (the widely used Al 2024-T3) and an aluminium-copper alloy from series 7000 (Al 7075-T6).

Testing was performed on specimens treated with trivalent products for the chemical conversion coating process (Bonderite MN-T 65000), as well as on specimens treated with the old hexavalent conversion coating, in order to estimate correction factors for basic fatigue properties.

The main results for the selected materials are shown in Figure 3.12.

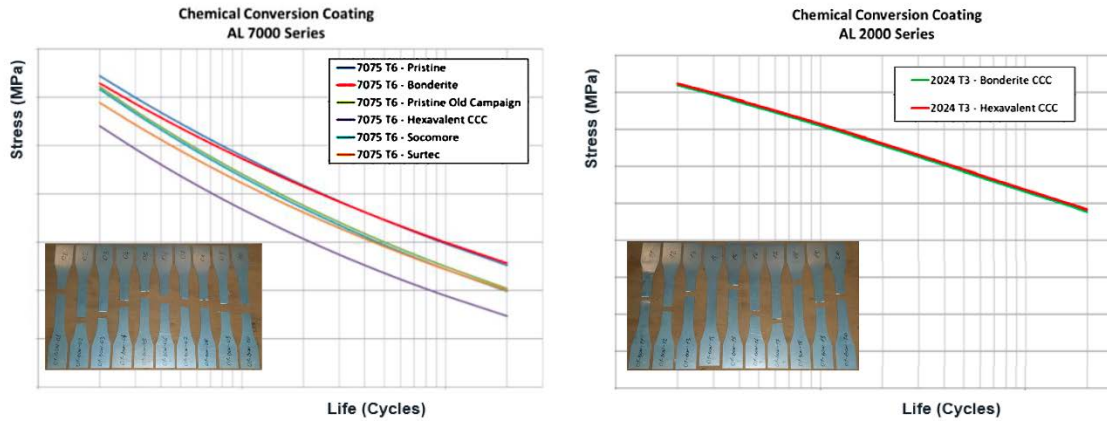


Figure 3.12 Results of fatigue tests on tri-valent and hexavalent chromium chemical conversion coatings on Series 2000 and 7000 aluminium alloys.

The test results show that the new Chemical Conversion Coating process based on Bonderite MN-T 65000 does not adversely affect the basic fatigue characteristics of the two aluminium alloys. This demonstrates compliance with CS 25.571 Amendment 24 and therefore justifies replacing the hexavalent chemical conversion coating.

3.3.2 Corrosion Monitoring: a possible solution (Leonardo Helicopter Division)

Corrosion is a significant issue for defense and civil organizations that maintain high-value assets and infrastructure. Improved corrosion management is also important for safety reasons, making it a shared responsibility in both military and civil aviation.

For helicopters, typical corrosion scenarios arise from pre-corrosion due to the manufacturing process (e.g. etching for surface treatment or bonding), or in-service corrosion (often due to improper coupling of materials or protection degradation/damage). The number of corroded items increases with the size and age of the fleet and the amount of exposure to aggressive environments.

In this context, the Leonardo Helicopter Division has set up a testing programme to evaluate the use of corrosion monitoring sensors developed by LUNA. The proposed sensors, shown in Figure 3.13, monitor both free corrosion of a single material and galvanic corrosion arising from the coupling of two different materials. Environmental parameters such as temperature and relative humidity are also recorded. The sensors operate using an autonomous power supply provided by an on-board battery, which is sized to last five years with a data sampling interval of 60 minutes.



Figure 3.13 Corrosion monitoring sensor proposed by LUNA.

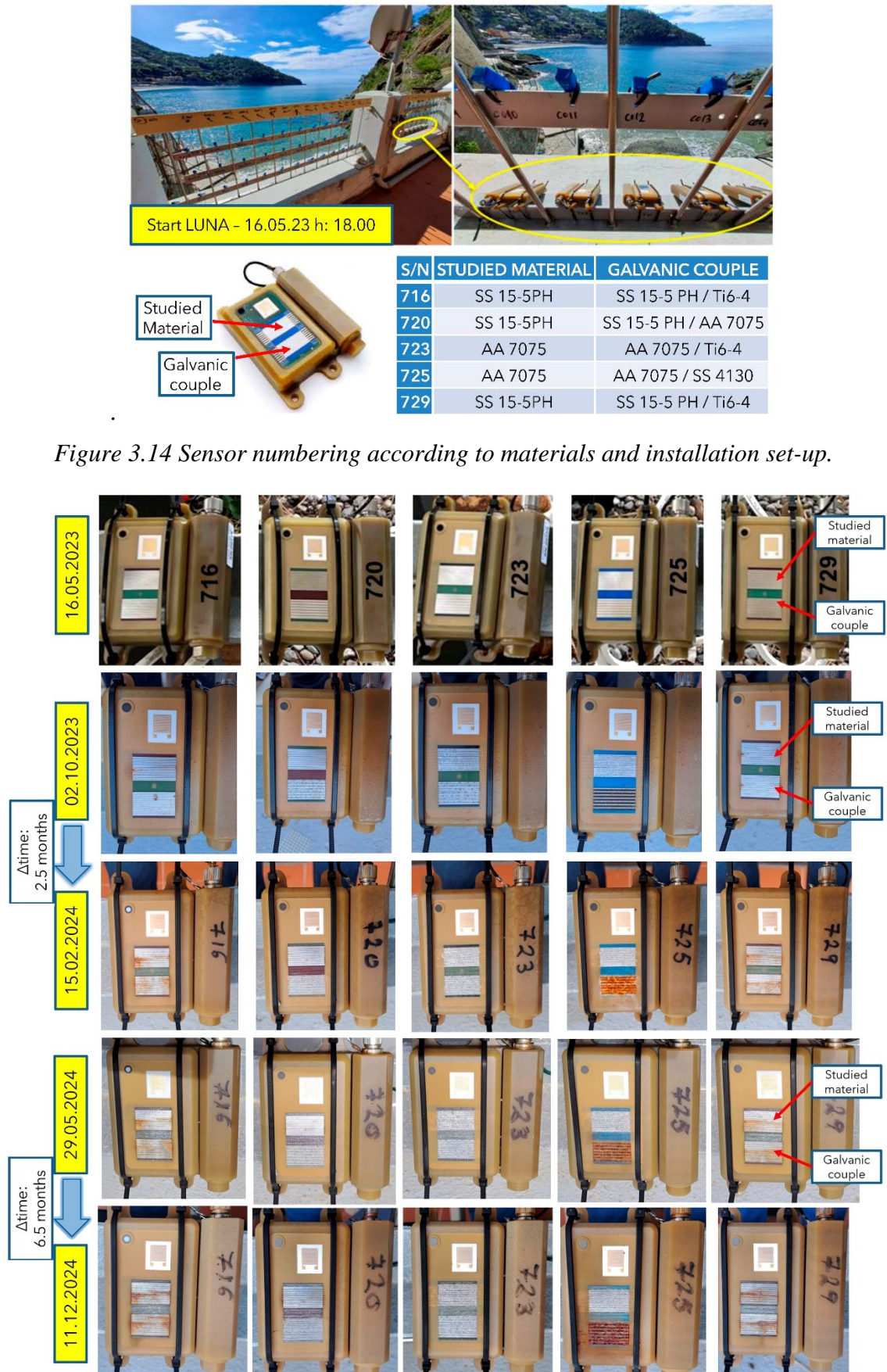


Figure 3.15 Visual history of corrosion revealed by the sensors at increasing exposure times

To assess their performance in an operating environment relevant to helicopters, five LUNA sensors were installed on the seafront terrace of the MARECO CNR ICMATE station in Bonassola in May 2023. They were monitored until November 2024. The sensors, produced by the LUNA company, were designed to monitor materials and material couplings, as shown in Figure 3.14.

Qualitative considerations of the state of free and galvanic corrosion were performed on the sensors through visual and periodic inspections at different exposure time intervals, as shown in Figure 3.15.

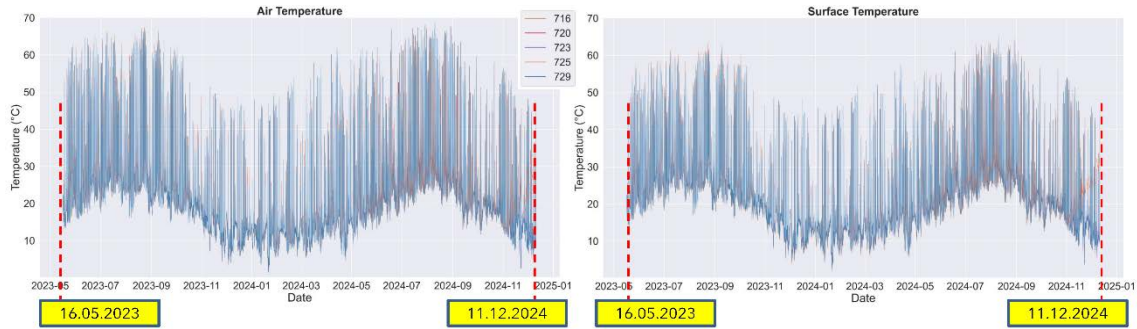


Figure 3.16 Air and surface temperature recorded by all the sensors.

As the corrosion phenomenon is directly related to atmospheric parameters, these were monitored throughout the exposure period. The data confirms that all the sensors recorded the same air and surface temperatures (see Figure 3.16).

The temperatures acquired by each sensor were higher than the air temperature measured by a nearby weather station, probably due to solar irradiance heating the devices. This resulted in lower relative humidity.

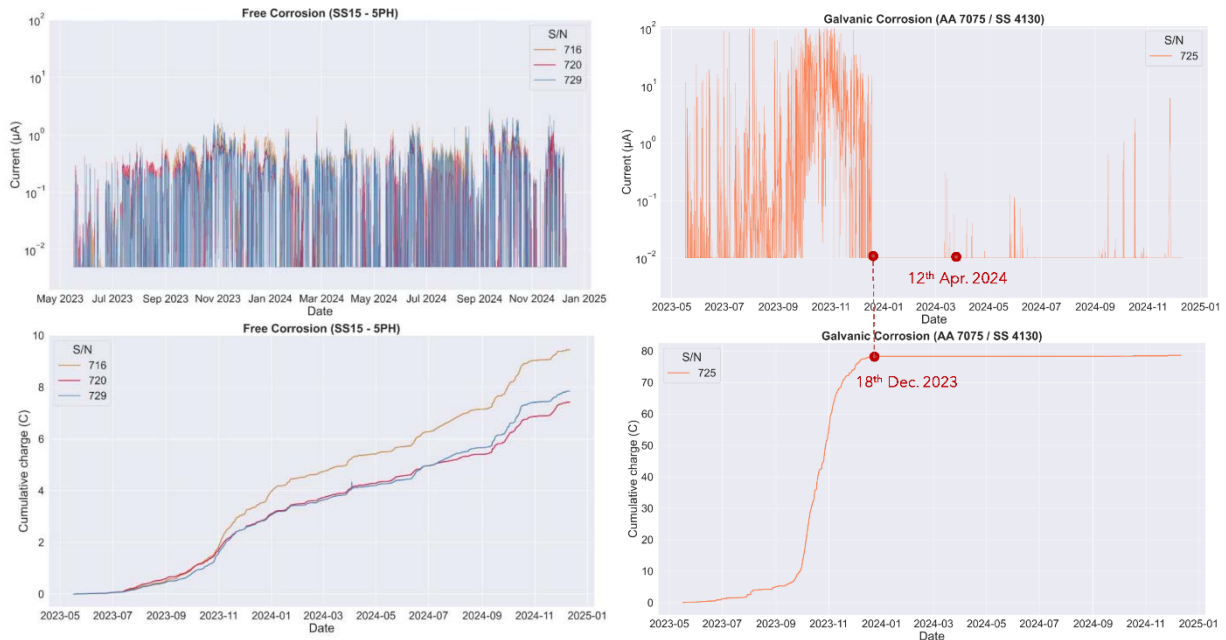


Figure 3.17 Examples of corrosion data recorded: free corrosion of SS (left) and galvanic corrosion of the AA7074/SS4130 coupling (right).

Free corrosion plates made of the same material exhibit a comparable corrosion behaviour, as illustrated in the example shown Figure 3.17 (left). The trend of cumulative charge is qualitatively similar. Reaching a plateau in cumulative charge is related to the formation of coherent corrosion products, which slow down the process.

Figure 3.17 (right) shows an example of the readings for monitoring galvanic corrosion. A saturation tendency can be seen in the interruption of the current signal and the beginning of the cumulative charge plateau. The free and galvanic corrosion plates of the sensor were cleaned on 12 April 2024 to check for reactivation, which did not occur. The data in Figure 3.17 on the right show a fast galvanic corrosion process, indicating a very detrimental coupling between the AA 7075 aluminium alloy and the SS 4130 steel.

Preliminary results collected and analysed during the tests showed that LUNA sensors are a promising solution for addressing the problem of corrosion monitoring and are worth considering as an advanced system for improving maintenance operations. Further investigation is planned, involving the installation of LUNA sensors on two Leonardo helicopter prototypes.

4 FATIGUE AND DAMAGE TOLERANCE OF COMPOSITES

4.1 Fatigue in Adhesively Bonded Joints (Univ. of Bologna)

A study on fatigue crack growth in bonded specimens with a bolted Disbond Arrest Feature (DAF) is underway at the University of Bologna's Forlì Campus. Preliminary results have already been presented in previous editions of the National Review.

The research involves Cracked Lap Shear (CLS) testing, with an Hi-Lok installed in the centre. Two-dimensional (2D) models have been developed that can accurately reproduce the observed fatigue disbonding and capture the disbond arrest provided by the DAF. However, since the 3D behaviour observed in experimental tests shows additional features, a 3D model has been developed with the relevant UMAT subroutine to enable further research into the behaviour of the crack front in the presence of a disbond arrest feature. A 3D version of the UMAT that implements the constitutive equations for the adhesive layer has also been developed.

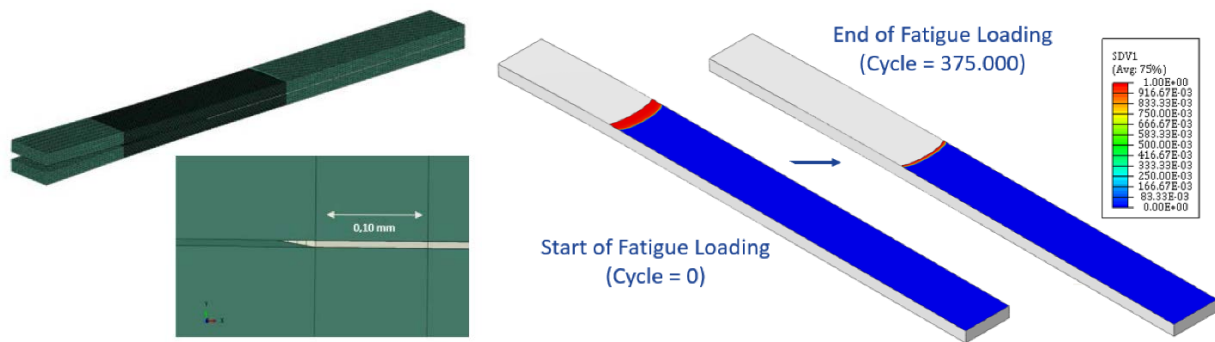


Figure 4.1 A DCB 3D model (left) and an example of the results of delamination growth (right).

Standard cohesive elements with user-defined material properties, endowed with both static and fatigue damage modelling capabilities, are employed to model the adhesive layer in 3D.

Paris' Law Parameters for crack propagation $\frac{da}{dN} = C \left(\frac{\Delta G}{G_C} \right)^m$				
Specimen	Adhesive Thickness [mm]	Displacement Ratio (R)	C	m
G-002-II	0.275	0.29	1.4775	6.3322
G-010-II	0.285	0.036	0.58133	4.9545
H-002-II	0.195	0.036	0.4185	5.1144
H-003-II	0.135	0.29	2.4102	6.8236
H-004-I	0.245	0.61	72.4202	10.3649

G: 2 adhesive layers H: 1.5 adhesive layers

Table 4.1 DCB reference experimental dataset

Figure 4.1 shows a reference 3D model for a DCB analysis. Results obtained in terms of crack propagation under fatigue cyclic loading are shown in the same figure.

A set of DCB test simulations was run and compared to the relevant experiments to assess the validity of the proposed 3D modelling approach. The relevant experimental dataset is provided in Table 4.1. Figure 4.2 show an example of the results obtained (including results from 2D analyses) in terms of crack length as a function of the number of fatigue cycles.

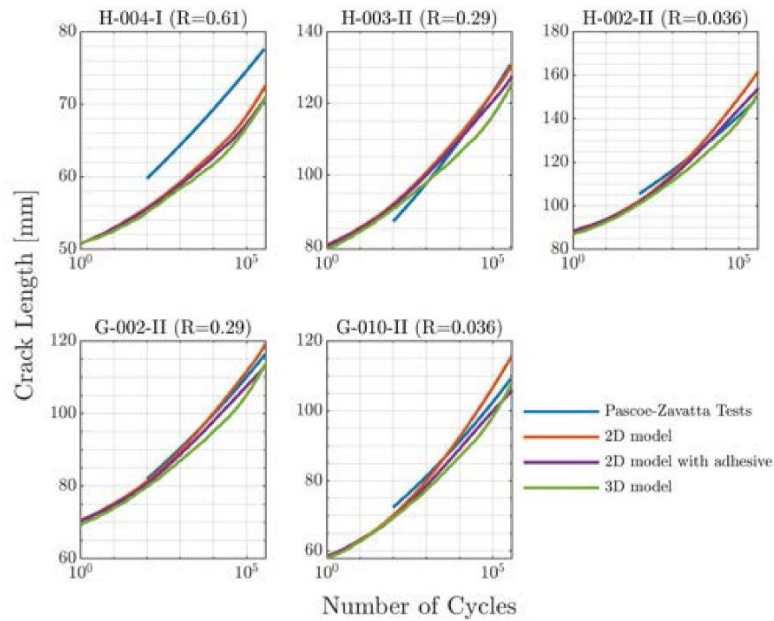


Figure 4.2 DCB results in terms of crack length versus the number of fatigue cycles.

In general, all simulated cases agree with the experimental data; the only exception is specimen H-004-1, which was probably due to it not being pre-cracked prior to fatigue testing.

4.2 Propagation of interface damage in adhesive joint and interlaminar layers in static and fatigue loading (Milan Polytech.)

The activities carried out at the Politecnico di Milano are an evolution of a research line on the damage tolerance of composite structural details, which has been reported on in previous editions of the National Review. Most of the analyses were performed using a hybrid-biphasic approach developed in-house on structural elements of increasing complexity, and the results obtained were compared with those from experiments carried out either internally or externally (through collaborations or open literature).

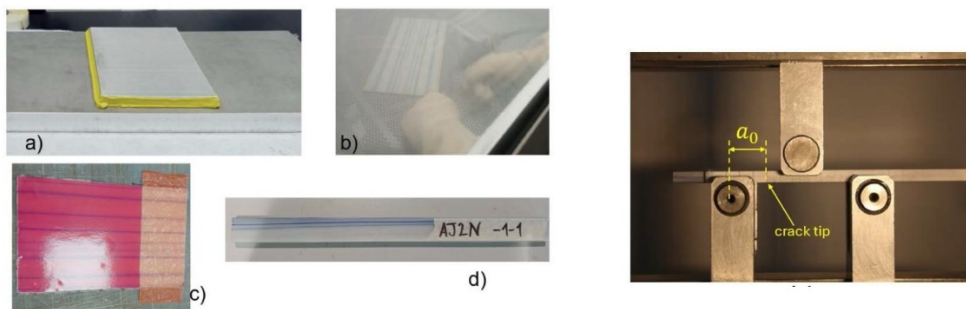


Figure 4.3 Fabrication and testing of ENF glass/epoxy specimens with a bonded interface.

The focus of the research activity on the adhesive interfaces was mode II behaviour, which was studied experimentally through static tests of ENF specimens. These specimens were fabricated from glass/epoxy UD composite plates that were hot bonded with an adhesive film (see Figure 4.6).

A numerical model was also developed that allowed multiple openings to be simulated. The adhesive layer was modelled using cohesive elements with a parametric traction-separation law, which offered the possibility of obtaining qualitatively different responses.

Figure 4.7 provides an overview of the finite element model of the ENF test setup and the possible alternative forms that the parametric traction-separation law can take.

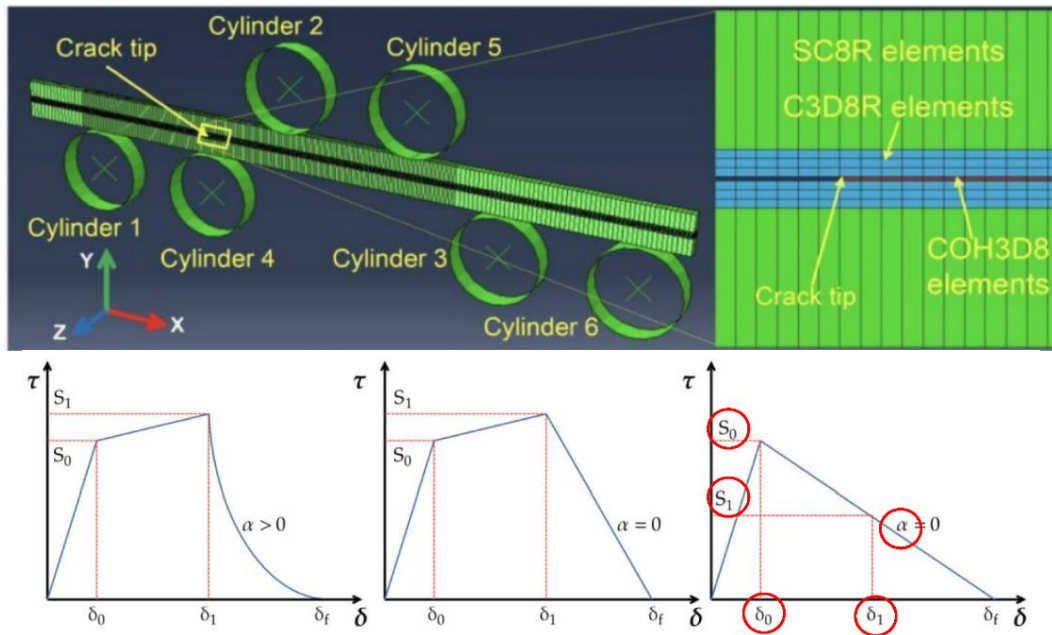


Figure 4.4 ENF setup FEM model and options for the traction-separation law

A machine learning approach was then used to identify the parameters that minimise the difference between the simulated and experimental force-displacement responses. Appreciable results were obtained for both the first and subsequent openings, as shown in Figure 4.8

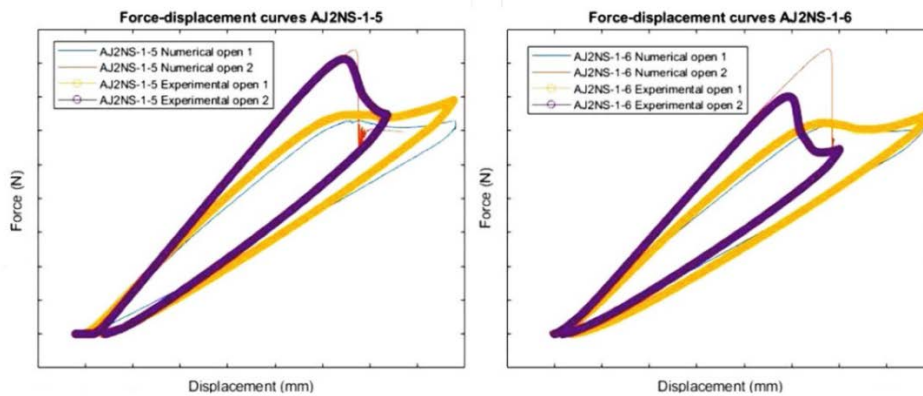


Figure 4.5 ENF tests: comparison of calibrated model response with experiments.

The Fatigue Delamination activity is inherently numerical and encompasses the development of a Fatigue Damage Accumulation Law with Internal Simplified Cyclic Loading (see Figure 4.9), similar to that proposed by Dr Davila and colleagues in [1]. This fatigue damage law was implemented in a VUMAT subroutine in Abaqus and used with standard cohesive elements.

The parameters were calibrated based on replicating the delamination propagation response of DCB and ENF specimens.

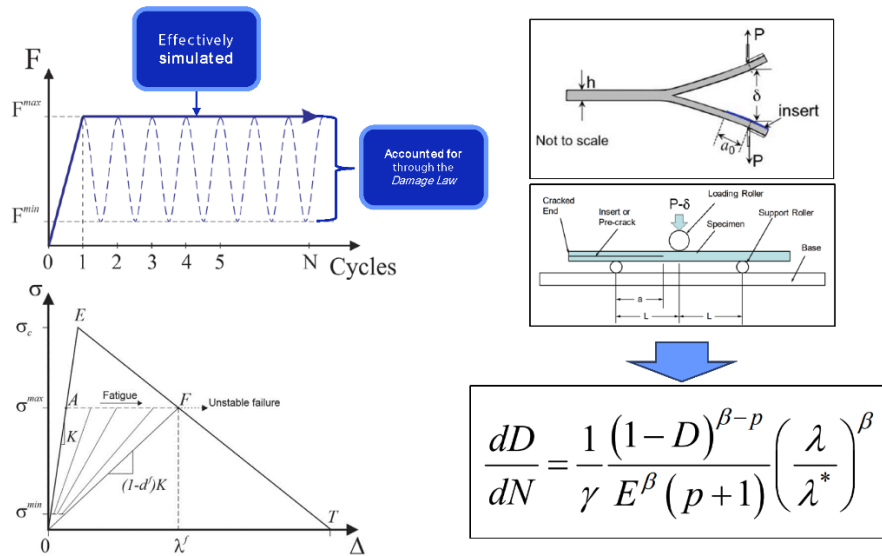
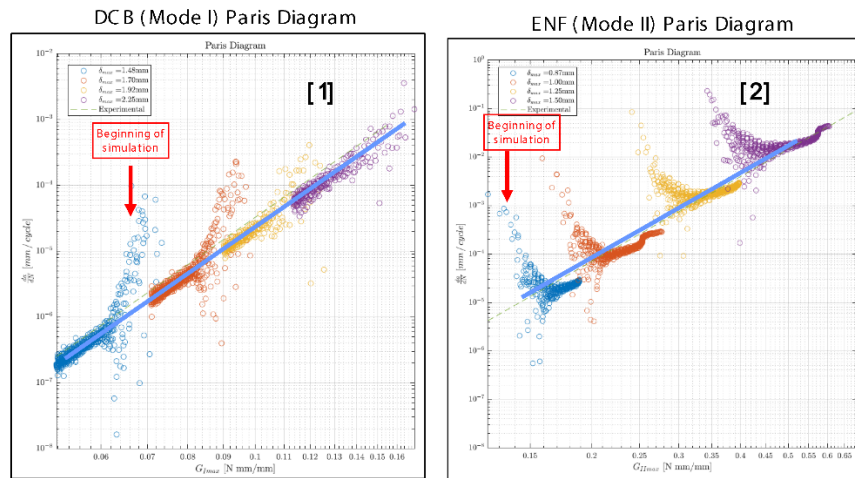


Figure 4.6 Key aspects of the Fatigue Delamination model

After calibration, the fatigue delamination model was verified using literature data by performing simulations at different initial severities (maximum cyclic load). Following an initial phase required to develop a suitable numerical process zone, the simulated delamination growth velocities stabilised at levels consistent with the experimental data as shown in Figure 4.10.



- [1] G. B. Murri (2012), *Evaluation of Delamination Onset and Growth Characterization Methods under Mode I Fatigue Loading*
 [2] R. Panduranga et al. (2017), *Mode-II total fatigue life model for unidirectional IM7/8552*

Figure 4.7 Fatigue Delamination model verification by comparison to literature data.

Further details can be found in the paper [2] to be presented at the 32nd ICAF Symposium.

4.3 Hygrothermal ageing and monitoring (Milan Polytech.)

Hygrothermal ageing represents a critical challenge for composite materials employed in aerospace applications. Over the years, several incidents have underscored the detrimental impact of moisture absorption on the mechanical properties of these materials. For instance, in 1989, a

Concorde aircraft suffered an in-flight separation of its honeycomb-bonded rudder due to delamination and adhesive bond deterioration caused by moisture ingress. Similar issues were reported in 1999 for CF-18 Hornet aircraft and in 2015 for an Airbus A310, where the combined effects of moisture and high temperatures led to component failures.



Figure 4.8 Issues related to Hygrothermal ageing: Concorde, 1989 (L); Airbus A310, 2015 (R).

The primary issue associated with moisture absorption in composites lies in its influence on the polymeric matrix. Humidity acts as a plasticizer, disrupting Van der Waals bonds and breaking cross-links between polymeric chains. This results in a degradation of mechanical properties, leading to interlaminar delamination, intralaminar cracking, and fiber-matrix interface failures. Consequently, monitoring moisture uptake in composite structures is essential to ensure their structural integrity and operational reliability.

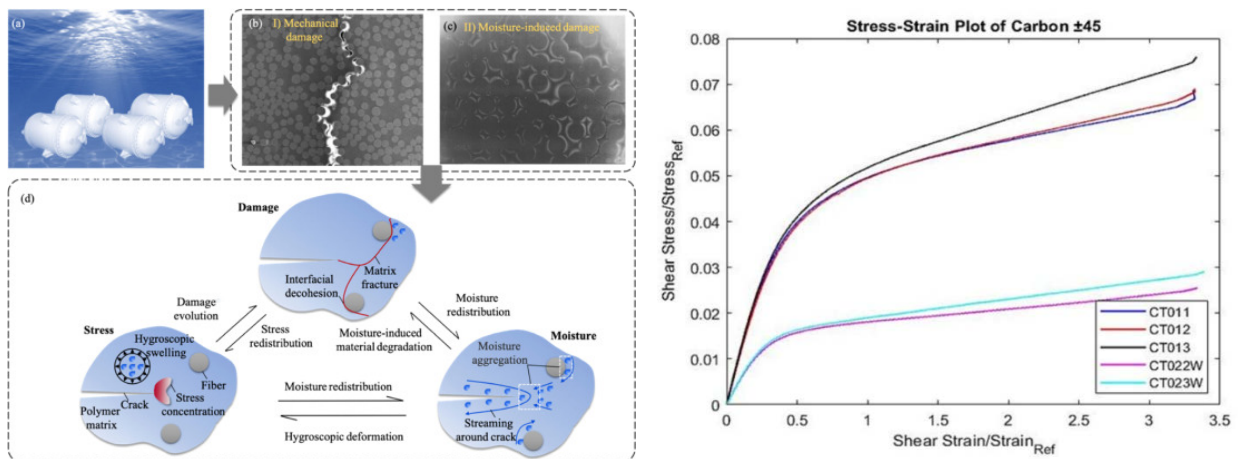
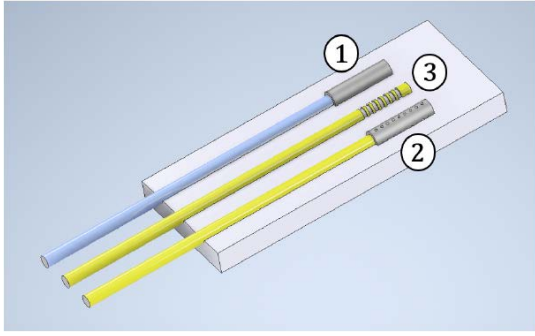


Figure 4.9 Effects of moisture uptake in composite materials.

Since humidity-related issues cannot be entirely mitigated through protective systems such as hydrophobic coatings—as evidenced by the aforementioned incidents—it is necessary to implement a Health and Usage Monitoring System (HUMS) and a Diagnosis, Prognosis and Health Monitoring (DPHM) system capable of measuring the moisture absorbed by the component and estimating its remaining useful life (RUL) taking into account the degradation of its mechanical properties given by moisture uptake.



$$\begin{cases} \frac{\Delta\lambda_1}{\lambda_{01}} = (\alpha_g + \xi)\Delta T \\ \frac{\Delta\lambda_2}{\lambda_{02}} = \left[(1 + p_e) \frac{A_c E_c \alpha_c + A_g E_g \alpha_g}{A_c E_c + A_g E_g} - p_e \alpha_g + \xi \right] \Delta T + \left[(1 + p_e) \frac{A_c E_c \beta_c}{A_c E_c + A_g E_g} \right] \Delta RH \\ \frac{\Delta\lambda_3}{\lambda_{03}} = \left[(1 + p_e) \frac{A_g E_g \alpha_g + A_c E_c \alpha_c + A_r E_r \alpha_r}{A_g E_g + A_c E_c + A_r E_r} - p_e \alpha_g + \xi \right] \Delta T + \left[(1 + p_e) \frac{A_c E_c \beta_c + A_r E_r \beta_r}{A_g E_g + A_c E_c + A_r E_r} \right] \Delta RH + (1 - p_e) \varepsilon_m \end{cases}$$

Figure 4.10 New FBG sensor to measure and decouple mechanical strain, thermal expansion and moisture swelling.

To this end, an optical fiber-based sensor has been developed, which, through modified Bragg gratings, can measure and decouple mechanical strains, thermal expansion, and moisture swelling using specially designed capillary tubes. The sensor can be embedded within materials, enabling measurements at internal points of the component.

The rise of bio-composites, incorporating organic fibers and matrices, further exacerbates hygroscopicity issues, making it even more critical to develop HUMS capable of tracking moisture absorption, updating mechanical properties, and predicting component lifespan.

4.4 Economic Impact Assessment of SHM Systems in Aeronautical Structure (Milan Polytech.)

This line of research, developed at Politecnico di Milano in collaboration with Leonardo Helicopters, aims to assess the cost-effectiveness of structural health monitoring systems.

SHMS can offer various advantages, such as online monitoring of structural integrity, eliminating the need to dismount structural elements for inspection, reducing manpower for inspection, increasing design allowable stress and reducing the weight of the structure, and predicting maintenance actions. Naturally, such positive aspects come at a cost, arising from issues in sensor integration, additional weight and cost, critical detection performance, and an overall decrease in the reliability of the aircraft.

A rational assessment of the cost/benefit ratio of such systems can be performed in four steps:

1) Recognition of a possible use for the SHMS, 2) Integration of the SHMS in the lifecycle, 3) Assessment of SHMS performance and 4) Assessment of the economic impact.

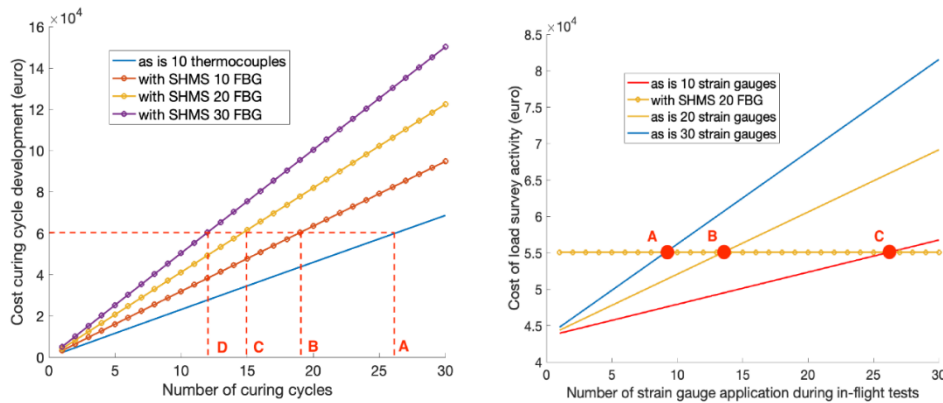


Figure 4.11 Examples of the cost/savings connected to the use of a SHMS.

Each aspect should be evaluated in at least two usage scenarios: at the beginning of the part/system's life ("Beginning of Life") and at the middle of its life, i.e. during normal use ("Middle of Life"). The Life Cycle Costing methodology compares two cases: an 'as is' case without SHMS, which provides a basis for actual incurred costs, and a SHMS case in which full integration of the system is envisaged.

An example of a "beginning of life" scenario is offered by the development of a new composite rotor blade. In this case, the expected benefits of an SHMS (embedded FBG optical system) can be realised during the blade curing cycle, during lab tests for blade certification, and during load surveys for final blade certification.

The expected benefits to be quantified are:

- better quality of temperature field;
- reduced number of trial curing cycles.
- better quality strain field and reduced number of tests;
- no need for strain gauges, since FBG is already present.

Figure 1 shows an example of the cost/savings connected to the use of a SHMS.

A middle-of-life comparison is more challenging. One possible solution is to set up the two cases for comparison so that they carry the same level of risk. This involves finding an SHMS inspection interval that carries the same risk as the "as is" case, and then performing an economic impact assessment of the two cases.

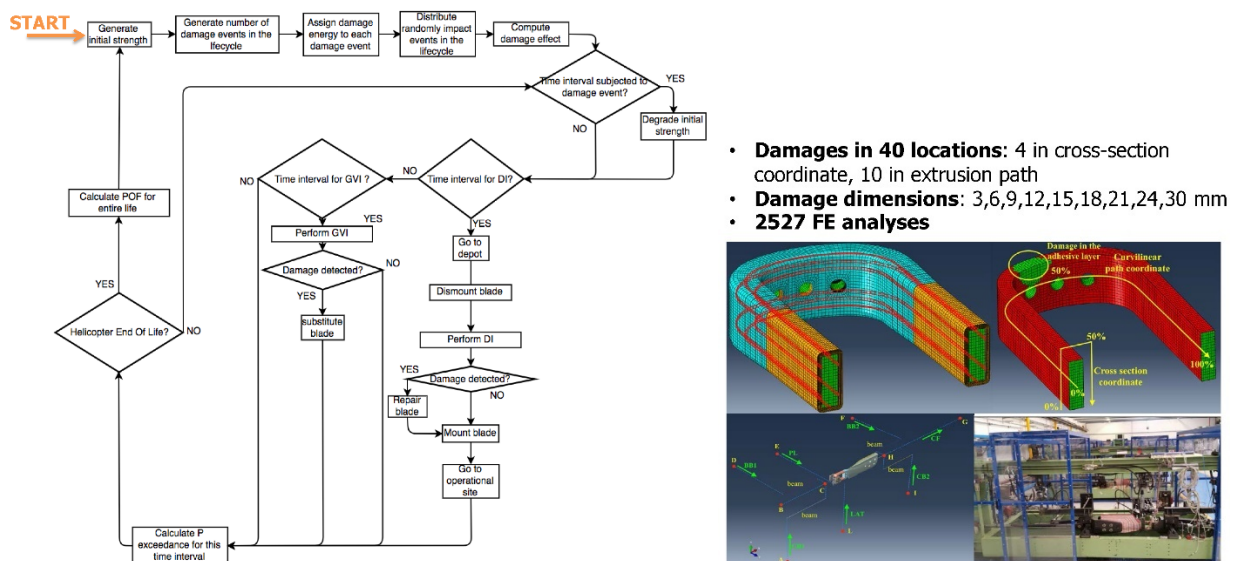


Figure 4.12 probabilistic damage tolerance analysis: methods and tools

A probabilistic damage tolerance analysis must be performed using appropriate models (damage injection capability) and numerical tools to evaluate damage threats in complex loading scenarios (the effects of damage and loads must be decoupled). A summary of the necessary steps and models is provided in Figure 4.14.

The economic assessment is then carried out. This is based on the concept of the net present value (NPV) of the two cases to be compared. Refer to Figure 4.13 for a working definition of NPV and for the relevant values in the example of the rotor blade.

Net Present Value (NPV)

$$NPV = \sum_{time}^{life\ span} \underbrace{CF}_{\text{Cash flow}}(time) (1 + \underbrace{r}_{\text{Discount rate}})^{-time}$$

NPV for the testcase (SHMS II @ 1070 FH)

Highly sensitive to *repair time, cost of spare part*

$$NPV^{as\ is} = 189.4\ k\text{€} \quad NPV^{SHMS} = 272.6\ k\text{€}$$

Figure 4.13 Definition of the Net Present Value (NPV).

The global results of the economic impact assessment are shown in Figure 4.13, while Figure 4.14 shows the partition of the Net Present Value for the two cases relevant to the blade example.

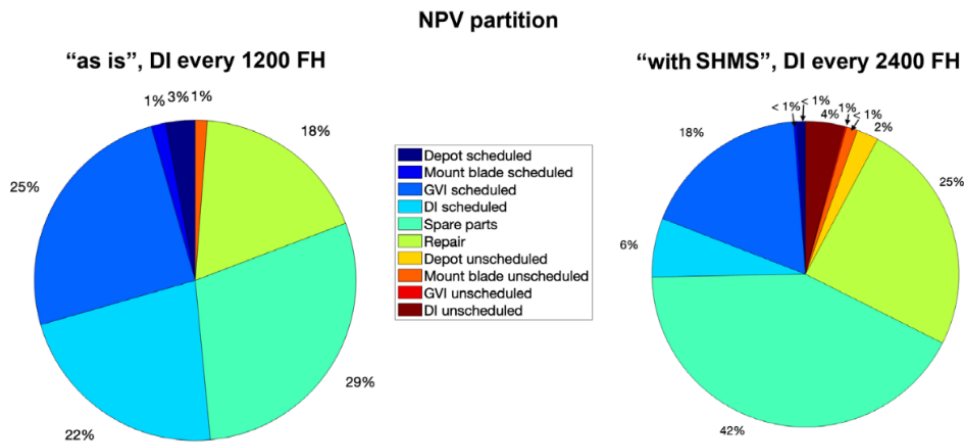


Figure 4.14 Partition of the Net Present Value for the two cases relevant to the blade example.

The savings in scheduled maintenance in the "as is" scenario are offset by the higher cost of spare parts and repair operations in the "with SHMS" scenario. Different outcomes are expected for different parts (internal elements, since they are hard to disassemble and less prone to damage), or if SHMS implementation improves (reduced number of sensors, reduced sensor integration complexity, increased system reliability).

4.5 CFRP Fracture Properties for Crash Application (Univ. of Bologna)

Combined numerical and experimental research activities are ongoing at the University of Bologna's Forlì campus to calibrate and utilise the Waas-Pineda damage model with the ESI-VPS software. The Waas-Pineda damage model is available in the software for unidirectional (UD) and fabric tapes, but a suitable calibration procedure is necessary to achieve optimal results in crashworthiness simulations.

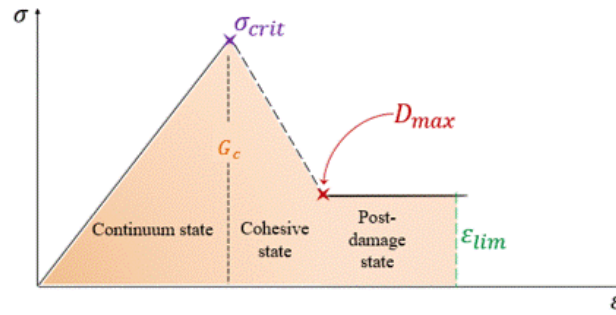


Figure 4.15 Wass-Pineda model stress-strain response: calibration parameters.

The calibration procedure is organized into the following steps:

- Obtain the relevant failure stresses from tests.
- Use these as stress thresholds for damage initiation in tension, compression and shear loading conditions (see Figure 4.15).
- Evaluate the ERR for the interfaces from the DCB and ENF tests.
- Calculate the intralaminar ERR from the compact tension (CT) and compact compression (CC) tests.
- Use the intralaminar ERR values to run a simulation and check whether they are adequate for the mesh dimensions. If not, use the simulation results as a starting point for calibration.
- Tune the stress degradation limit and the equivalent strain limit (see Figure 4.15) to ensure numerical stability.

- Fracture toughness is calculated with the ASTM E399 modified method for CT and with the Compliance Calibration method for CC tests
- Specimens: $[90/0]_{2s}$

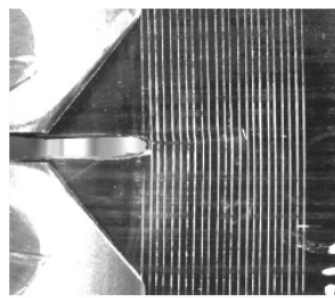
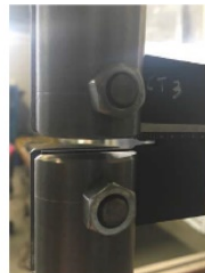


Figure 4.16 Compact Tension/compression experiments to determine intralaminar ERR.

The intralaminar fracture toughness is evaluated using the modified ASTM E399 method for CT specimens and the compliance calibration method for CC specimens (see Figure 4.16).

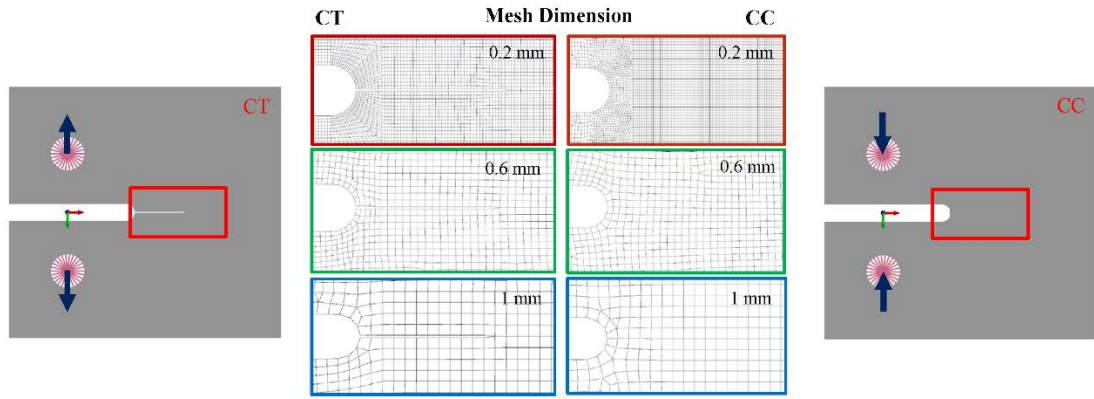


Figure 4.17 Models of Compact Tension/Compression specimens for calibration.

Calibration has been performed using CT and CC specimen models with increasing mesh densities, as shown in Figure 4.17. A summary of the calibration procedure results for CT and CC specimens is shown in Figure 4.18.

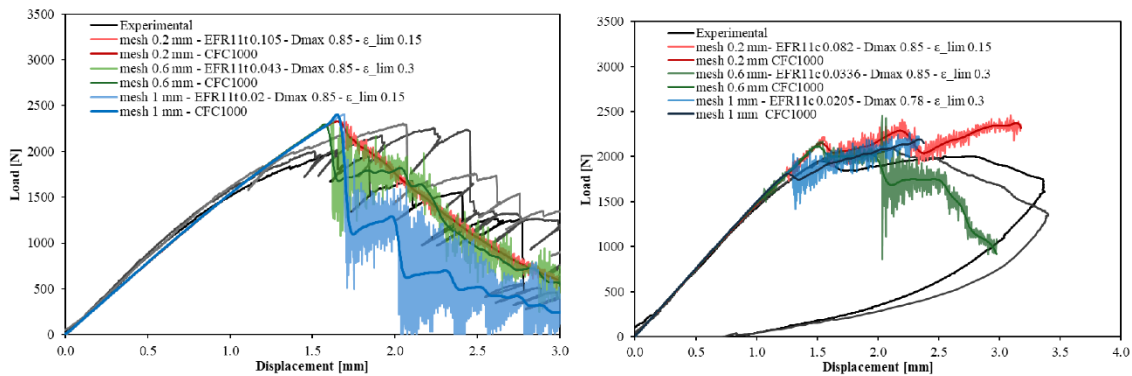


Figure 4.18 Calibration results: Compact Tension (left) Compact Compression (right).

A complex crash simulation model, for which experimental data were available for comparison, was then developed to verify the calibration of the WP damage model (see Figure 4.19).

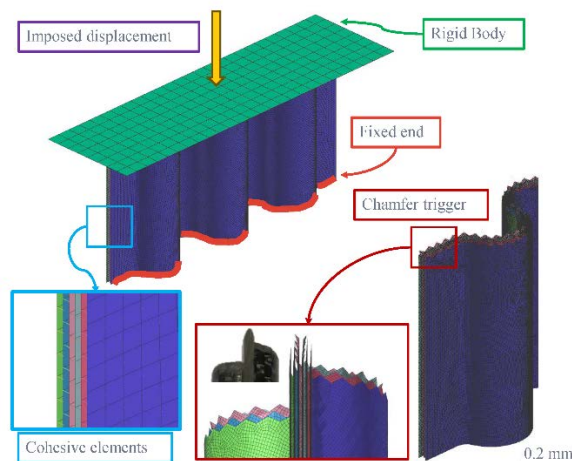


Figure 4.19 Crash simulation model to verify the calibration of the WP damage model.

The results of the simulations for different mesh sizes are shown in Figure 4.20, where the results of the uncalibrated model are also reported and compared with the experimental data.

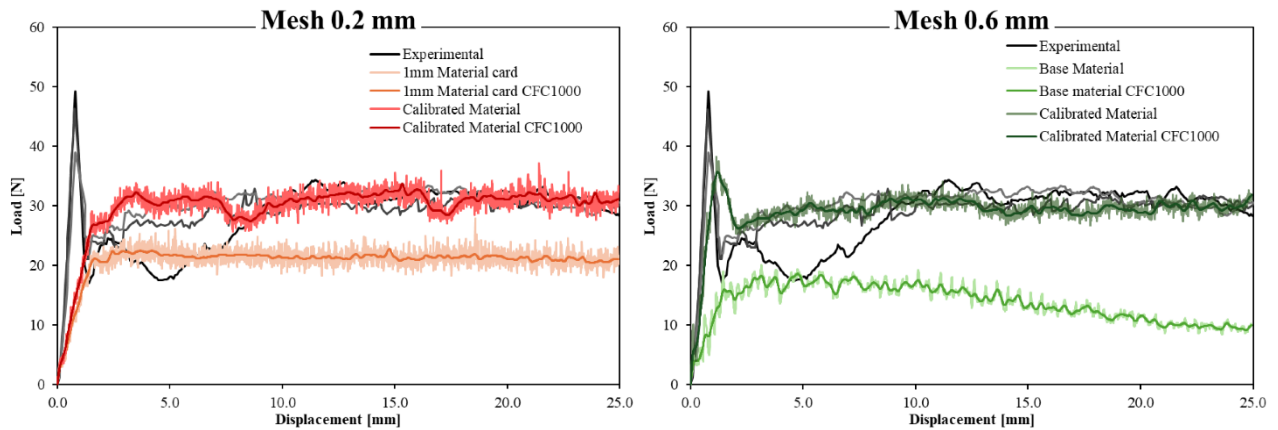


Figure 4.20 Crash simulation model results: sensitivity to mesh size and calibration

Clearly, the model is mildly sensitive to mesh size, provided it is sufficiently small, and calibration is essential for obtaining results that match the experiments reasonably well.

4.6 Interlaminar properties of Various Composite Materials (Univ. of Pisa)

The reported activities are part of an experimental programme carried out by the University of Pisa, in collaboration with Leonardo Helicopters and the Polytechnic of Milan. The programme covered various factors that can affect the interlaminar strength or delamination toughness of composite interfaces. The results presented below are relevant to two main areas: The effects of high temperatures on the strength and toughness of ply interfaces (in some cases including and adhesive layer), and the behaviour of delaminations developing at hybrid and/or angle ply interfaces (bonded by a co-cured adhesive layer).

Figure 4.21 shows the effect of high temperature (80°C) on conditioned carbon and glass fibre ILSS specimens (immersed in hot water at 70°C until saturated). A typical example obtained by testing the specimens at room temperature is shown on the left; the hot wet counterpart is shown on the right. RT tests show a brittle response, with a sudden drop in load when failure is reached. The CFRP specimens show significant delamination and fibre breakage at failure; the GFRP version fails more gently, with traces of fibre breakage on the tension side, but no delamination.

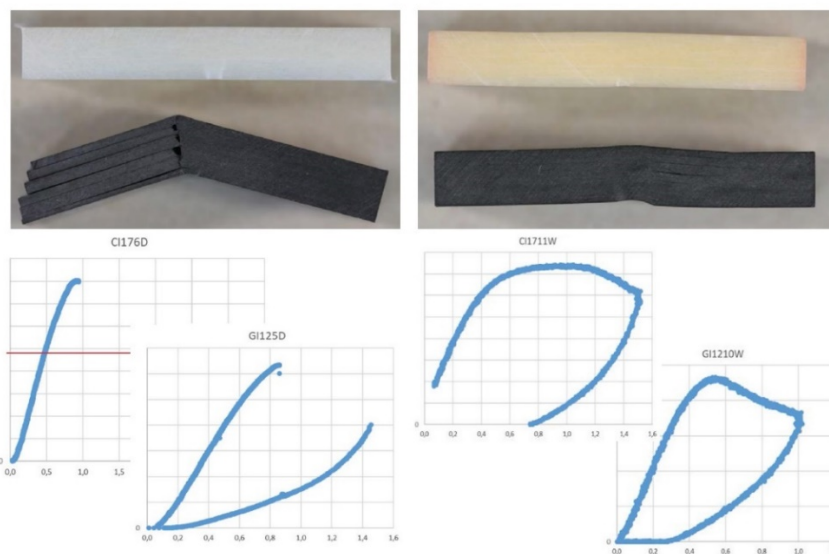


Figure 4.21 ILSS tests at different conditioning: RT (left) HW (right)

The HW test revealed more ductile behaviour, with large displacements prior to failure, which manifested as a gentle reduction in force at increasing displacements. In this case, the CFRP specimens exhibited local delamination, but it was less severe than in the RT case.

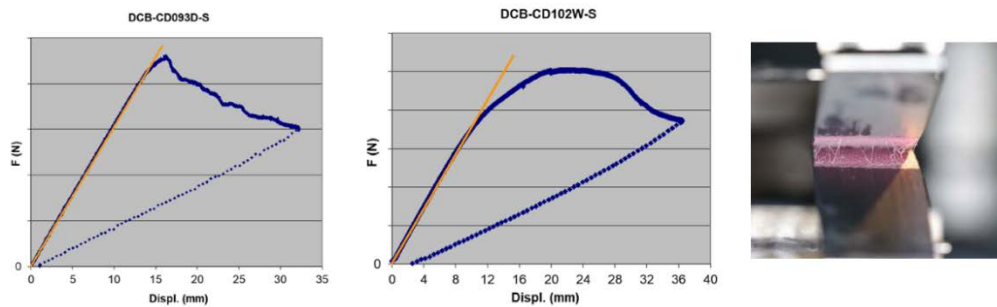
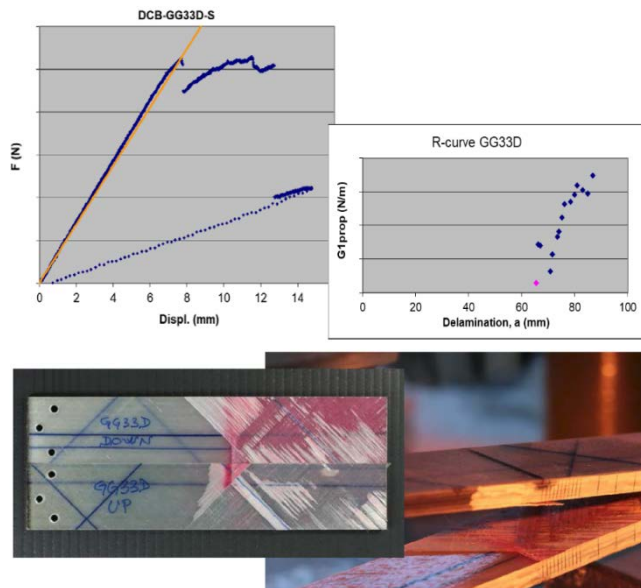


Figure 4.22 DCB tests on UD CFRP specimens at different conditioning: RT (left) HW (right)

Figure 4.19 shows a comparison of the behaviour of DCB tests on unidirectional (UD) carbon fibre reinforced plastic (CFRP) specimens with different conditioning when an adhesive layer is present at the interface. At room temperature, mild non-linearity is observed as the maximum load is reached. This behaviour is expected given the increased ductility and toughness induced by the presence of an adhesive layer. Humidity and high temperature enhanced this behaviour, and the deviation from linearity of the load displacement response was anticipated, and consequently, toughness diminished, regardless of the evaluation criterion used.



GG stratification:	GC stratification:
G_0_2	C_0_2
G_+/-45_2	G_+/-45_2
G_+/-45_2	G_+/-45_2
C_0_8	C_0_6
C_90_2	C_90_2
C_0_8	C_0_6
G_-/+45_2	G_-/+45_2
G_-/+45_2	G_-/+45_2
G_0_2	C_0_2
Insert/adhesive	Insert/adhesive
G_+/-45_2	G_+/-45_2
G_0_2	C_0_5
C_0_1	G_+/-45_2
G_-/+45_2	C_0_3
C_0_7	C_90_2
C_90_2	C_0_3
C_0_7	G_-/+45_2
G_+/-45_2	C_0_5
C_0_1	G_-/+45_2
G_0_2	Code on this side
G_-/+45_2	
Code on this side	

Figure 4.23 DCB tests on Hybrid Specimens with adhesive at the interface (GG stratification)

Figure 4.20 and Figure 4.21 show examples of the results obtained when testing hybrid specimens in a DCB setup. The stratifications used to produce the specimens are shown in the table in Figure 4.20. In the GG stratification, there is an angle ply interface, but the adhesive is contained between two layers of the same glass material, whereas in the GC stratification, the layer with fibres aligned to the long sides of the specimens is replaced with a carbon fibre layer. In both cases, the

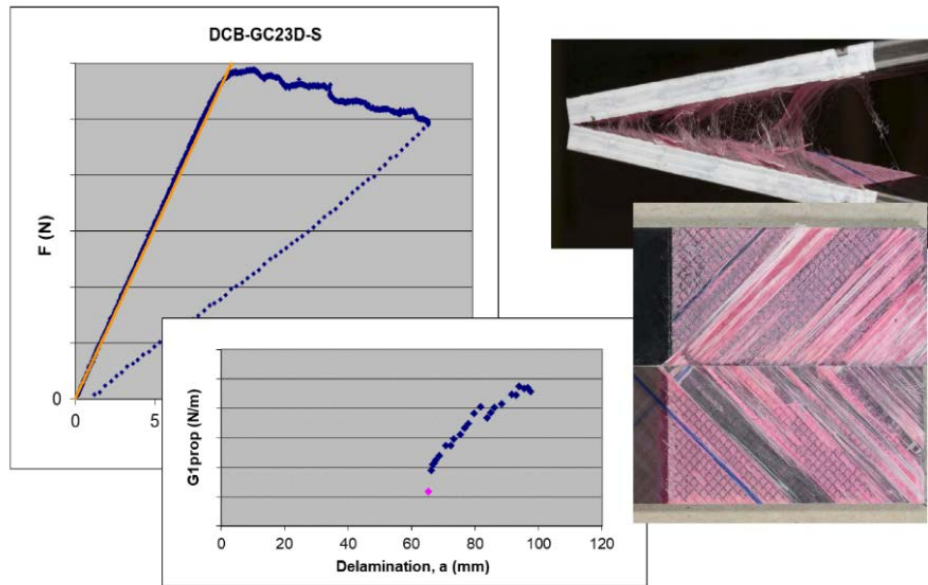


Figure 4.24 DCB tests on Hybrid Specimens with adhesive at the interface (GC stratification)

In both cases, the behaviour is similar to that expected from a standard specimen when considering the load-displacement response. However, closer inspection of the tests reveals a steep R-curve, which, when interpreted as for monomaterials, indicates non-stabilised delamination growth with varying critical ERR. Moreover, upon opening the specimen, it became clear that the interface had failed in a highly complex manner, involving delamination migration and intralaminar damage. This makes the use of the test questionable for characterising the interfaces of hybrid specimens (even in the presence of the adhesive).

5 NDI METHODS

5.1 Methodology for Detectable Crack Length determination (Leonardo Helicopter Division)

According to Leonardo Helicopters' experience, a detectable crack length of 5 mm was considered adequate for detailed visual inspections and accepted by the authorities for calculations performed on recent products. However, during discussions with Certification Authority Specialists, it was questioned whether the value used in the standard approach to crack propagation analysis was adequate and reliable for all critical locations, without taking into account specific aspects related to how the inspection task is carried out in a real environment. Following this discussion, a new methodology was defined to take into account the main parameters that can impact crack length detectability.

The methodology focuses on detailed inspection tasks. A detailed inspection is an intensive examination of a specific item, installation, or assembly to detect damage, failure, or irregularity. This could include a tactile assessment, whereby a component or assembly is checked for tightness or security. Available lighting is normally supplemented with an additional light source at an appropriate intensity. Inspection aids such as mirrors and magnifying lenses may be necessary. Surface cleaning and elaborate access procedures may also be necessary.

View Rating	
0	Greater than 1.5 meters *
1	Between 1 meter and 1.5 meters
2	Between 0.5 meters and 1 meter
3	Lower than 0.5 meter and as close as needed (Unrestrained)

Congestion Rating		Size Rating	
1	Congested	0	Large Surfaces or Fittings *
2	Moderate Congestion	1	Medium Size Fittings - to include portions of frames, spars, ribs and intercostals or stringers (i.e. area up to 13 squared decimetres**)
3	Clear Area	2	Small Fittings / Small Area (i.e. area up to 3 squared decimeters***)

Lighting Rating		Surface Rating	
0	External or internal dull light *	0	Polyurethane finish or equivalent elastic surface coating *
1	External of aircraft in full daylight, inside aircraft with artificial light	1	Areas or items liable to be covered in sealant or subject to excessive grease, oil or dirt contamination
2	Concentrated light as required	2	Clean areas

Table 5.1 Ratings for single parameters that impact the detectability of cracks.

The following parameters, which can impact the detectability of cracks, have been considered:

- View distance.
- Congestion of the area to be inspected.
- Size of the location to be inspected
- Lighting conditions
- Surface condition

A rating is provided for each parameter, which are then combined into a global 'rating matrix' using a guided, step-by-step procedure. Finally, a detectable crack length is established as a function of this global rating. A rating index equal to zero is related to conditions that are not

applicable. A brief description of the parameters that can affect the detectability of cracks follows. Their respective ratings are defined in Table 5.1.

View distance. This is related to the distance between the inspector's eyes and the location of the part to be inspected.

Congestion of the area to be inspected. The ability to detect a crack during a field inspection can be affected by obstructions in the area of the maintenance task that can interfere with the required operations, or by the complexity of the item to be inspected.

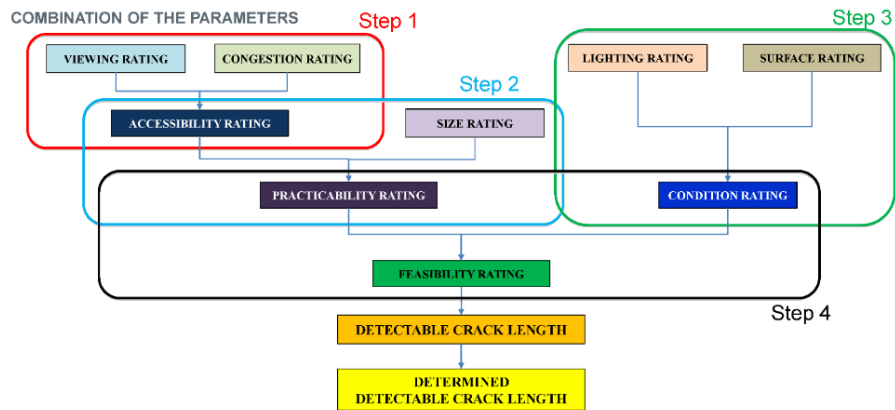


Figure 5.1 Flow diagram to combine the single parameters.

Size of the location to be inspected. The ability to detect cracks in structural components during a field inspection can be affected by the size of the part being inspected. (Notes: * Larger surfaces or fittings are not applicable due to typical helicopter dimensions. ** The area of an A3 sheet of paper. *** The area of an A5 paper sheet.)

Lighting conditions. The ability to detect cracks during a field inspection can be affected by external lighting conditions and the possibility of using artificial light for the specific maintenance task.

Surface condition. The ability to detect cracks during a field inspection can be affected by surface conditions (e.g. the presence of primer or sealant) or finishes (e.g. roughness, the presence of shot peening or other mechanical treatments). (Notes: * For these cases, a Special Detailed Inspection using eddy current methods must be carried out, and the proposed methodology is not applicable.)

Accessibility Rating		Congestion Rating			Practicability Rating		Accessibility Rating		
		Congested	Moderate Congestion	Clear Area			1	2	3
View Rating	1m / 1.5m	1	1	1	Size Rating	Medium	1	1	2
	0.5m / 1m	1	2	2		Small	2	2	3
	as close as needed	1	2	3					
Condition Rating		Lighting Rating			Feasibility Rating		Condition Rating		
		Day-Light	Concentrated Light				1	2	3
Surface Rating	Not Clean	1	2		Practicability Rating	1	1	2	3
	Clean	2	3			2	2	4	5
						3	3	5	6

Table 5.2 Ratings for combined parameters that impact the detectability of cracks.

The combined parameters are then obtained using the flowchart in Figure 5.1. The values of the combined ratings are given in Table 5.2.

The Accessibility Rating is obtained by combining the View and Congestion ratings. This is then combined with the Size rating to obtain the Practicability rating, which indicates how easy it is to perform the inspection task. The Condition rating is obtained by combining the ratings associated with Surface and Lighting conditions. The practicability and condition ratings are then combined to obtain an overall index associated with the feasibility of the inspection task. The higher the feasibility rating index, the greater the probability of detecting a smaller crack length.

The proposed values for the detectable crack length vary from 5 mm to 30 mm. These values were chosen according to the following considerations:

- 5 mm is currently used in crack propagation analysis to evaluate inspection intervals. This value is associated with small, clean, uncongested and well-illuminated areas that are inspected as closely as necessary. This type of inspection is considered to have detection capabilities similar to those of an SDI with a borescope, for which a value of 5 mm is considered conservative.
- 8 mm is consistent with the survey reported in DOT/FAA/AR-96/65.
- 30 mm is consistent with the Legacy AW criteria for visual inspection of dull paint surfaces.

Intermediate values can be obtained by applying a suitable law.

The values obtained using this methodology may underestimate or overestimate the actual detectable crack length in specific cases, such as cracks near an edge or partial through cracks. For these cases, the values to be used must be defined on a case-by-case basis.

Figure 5.2 shows examples of cracks with the related measured lengths. These values are consistent with those considered in the proposed methodology.

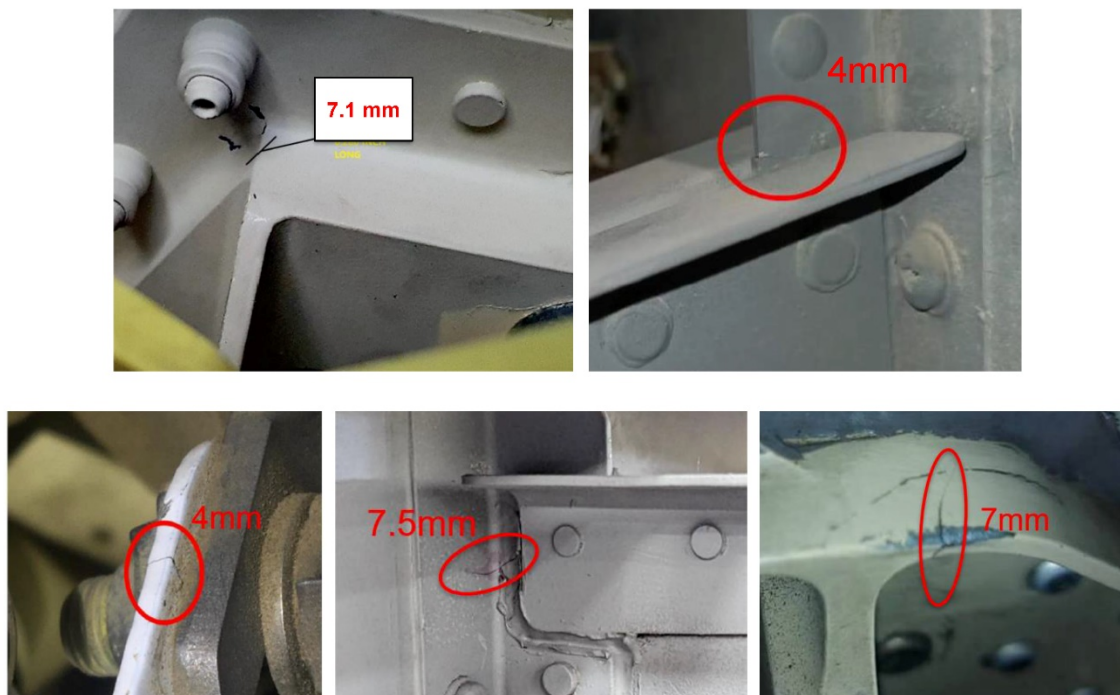


Figure 5.2 Examples of cracks with lengths consistent with those considered in the proposed methodology

6 AIRCRAFT FATIGUE SUBSTANTIATION

6.1 AW169 –Cross Tubes Fatigue Life Recalculation supported by HUMS data (Leonardo Helicopter Division)

The skid version of the AW169 helicopter was certified with a provisional life for the cross tubes, pending the completion of certification tests. A specific customer uses the helicopters in a way that results in an unusual landing/flight hour (FH) ratio due to a particular training activity for pilots. This meant that the cross-tube life expired before the certification tests were completed.

To avoid replacing the cross tubes, a detailed review of usage monitoring data was carried out using the HUMS system installed on the fleet. The aim was to define a more realistic usage for the parts, thus extending the authorised life.

The general process foreseen for this activity can be summarised into four steps:

- 1) Collection of HUMS data in terms of sinking speed.
- 2) Replacement of the theoretical sinking speed spectrum with the actual one.
- 3) Re-evaluation of damage based on actual usage.
- 4) Definition of an equivalent number of landings to replace the real number reported in the component log cards.

The calculation approach to standard safe life is articulated as follows:

- The life of the landing gear is evaluated using a theoretical spectrum based on landing and ground handling conditions.
- the theoretical spectrum is parameterised in terms of helicopter weight at landing and sinking speed.
- A conservative statistical distribution of the two parameters is considered, including limit load values.
- The distribution is grouped into corner points of predefined weight bands.
- The loading conditions used to calculate stress in critical sections are derived from models calibrated on the basis of drop tests.

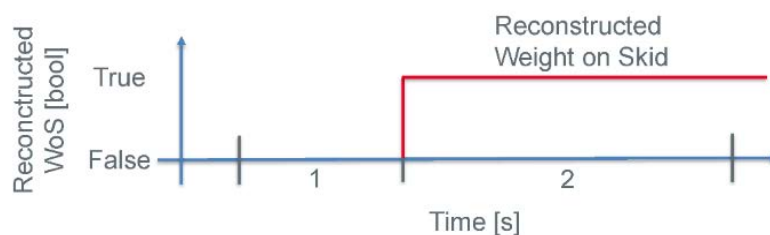


Figure 6.1 Observation windows for detecting sinking speed and weight at landing

A specific HUMS data analysis has been developed in order to extract sinking speed and weight.

As the Weight on Skid (WoS) signal is computed by a robust on-board system rather than acquired by a physical sensor, the switch from “false” (flight) to “true” (ground) is delayed by a few seconds with respect to the actual landing instant. Therefore, the landing instant must be computed using an alternative method, i.e. identifying the landing manoeuvre using the Machine Learning – Flight Condition Recognition algorithm and selecting the instant at which the collective drops below 10% and remains below 1% thereafter. Once the landing instant has been identified, an observation window of one second before and two seconds after is set (see Figure 6.1). The minimum negative vertical speed in the window is identified as the sinking speed, while the maximum weight is extracted as the relative landing weight.

The actual sinking speed distribution was evaluated using HUMS data from a selection of landings carried out by the customer fleet; data is shown in Figure 6.2.

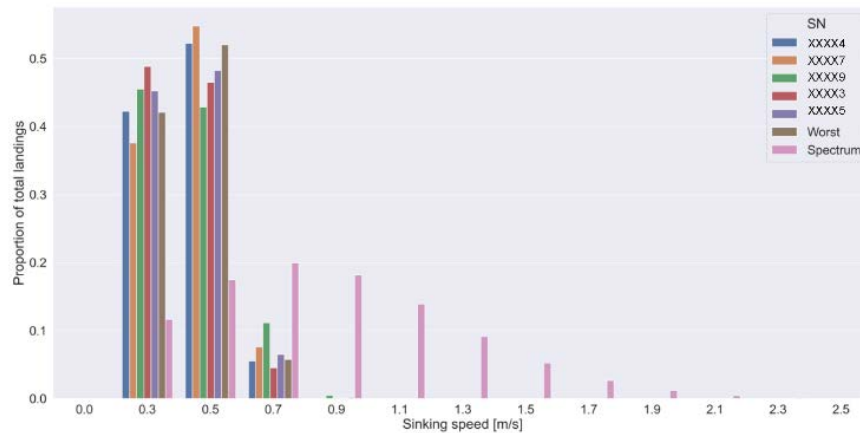


Figure 6.2 Actual distribution of sinking speed compared to reference design spectrum

Comparing the sinking speeds with those considered for certification shows that the helicopters in the analysis are not being used as severely as expected.

The fatigue life calculation was performed using the same fatigue curves as in the certification process, with no changes to the weight distribution, and detailed sinking speed data from customer's helicopters (shown in Figure 6.3).

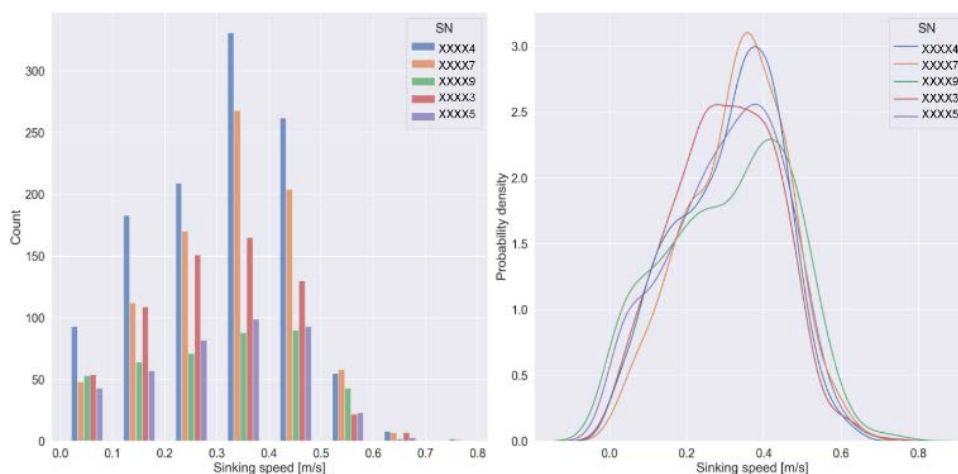


Figure 6.3 Sinking speed from HUMS: events in detailed bands and reconstructed PD

The results of the fatigue calculation are shown in Table 6.1 for the specific serial numbers of interest. For instance, considering S/N XXXX4, it can be seen that it has consumed 89.9% of the landings possible before reaching the part's life limit, and that the damage re-evaluated on the basis of actual usage is equivalent to 44.2% of the life limit.

Because of the proposed re-analysis, the real number of landings recorded on the component log card could be replaced by the equivalent number of landings evaluated. This approach ensures that the life reported in the ALS remains unchanged.

FWD CrossTube					
	Total Landings / Life	HUMS Landings / Total Landings	D HUMS	Residual Damage	Total Equivalent Landings for LogCard / Life
XXXX4	0.899	0.564	0.05	0.95	0.442
XXXX7	0.814	0.473	0.04	0.96	0.468
XXXX9	0.338	0.544	0.02	0.98	0.174
XXXX3	0.565	0.502	0.02	0.98	0.301
XXXX5	0.368	0.483	0.02	0.98	0.211

AFT CrossTube					
	Total Landings / Life	HUMS Landings / Total Landings	D HUMS	Residual Damage	Total Equivalent Landings for LogCard / Life
XXXX4	0.623	0.564	0.17	0.83	0.441
XXXX7	0.564	0.473	0.13	0.87	0.427
XXXX9	0.234	0.544	0.06	0.94	0.167
XXXX3	0.392	0.502	0.1	0.9	0.295
XXXX5	0.255	0.483	0.06	0.94	0.192

Table 6.1 Results of the cross-tubes fatigue re-analysis.

6.2 C-27J Fire Fighting Usage Preliminary Concept (Leonardo Aircraft Division)

This section reports on the activities of the Leonardo Aircraft Division aimed at developing a firefighting version of the C27J aircraft. The recent history of incidents involving firefighting aircraft highlights the importance of fatigue and damage tolerance aspects, given the higher severity of firefighting missions compared to those originally considered by OEMs. The main sources of information about firefighting aircraft usage and loads are summarised in Table 6.2.

Ref.	Year	Title	Author	A/C surveyed
1	2005	DOT/FAA/AR-05/35 - Consolidation and Analysis of Loading Data in Firefighting Operations Analysis of Existing Data and Definition of Preliminary Air Tanker and Lead Aircraft Spectra	FAA (study performed by Celeris Aerospace Canada Inc. over the previous 30 years, but with limited data)	<ul style="list-style-type: none"> Aerial Firefighters (MTOW 26,300 to 126,000 lbs) Firefighting - Lead aircrafts (MTOW 2,950 to 5,400 lbs) Crop spraying planes (MTOW 2,900 to 8,200 lbs)
2	2005	Advisory Circular - Certification of Large Aeroplanes in the Restricted Category, Used for Special Purpose Operations	Transport Canada	<ul style="list-style-type: none"> N/A → AC
3	2011	DOT/FAA/AR-11/7 - Usage and Maneuver Loads Monitoring of Heavy Air Tankers	FAA (study performed by Wichita State University in 2008-2009 fire seasons)	<ul style="list-style-type: none"> 12 P2-V (average TOW = 71,750 lbs) 6 P-3A (average TOW = 95,000 lbs)
4	2015	Airworthiness Assurance Guide for Aerial Firefighting and Natural Resource Aircraft	U.S. Forest Service Fire and Aviation Management	N/A → this document concerns an airworthiness approach for USFS-operated A/Cs
5	2018	2018 Transport Canada Delegates Conference Presentation - Conair «Special Mission» Airtanker STC modifications (mostly) from a Structures Perspective	Conair	<ul style="list-style-type: none"> L188, Q400, RJ85
6	2019	Flight Loads Spectra of a Fleet of Heavy Air Tankers	Wichita State University, US Forest Service (2015 to 2017 fire seasons)	<ul style="list-style-type: none"> BAe-146 (TOW=91,700 lbs) RJ-85 (TOW=97,000 lbs)
7	2021	Operational usage and flight loads analysis of C-130 aircraft used in aerial firefighting missions	S.J. Ali - M.Sc. Thesis Wichita State University (2016 to 2019 fire seasons)	<ul style="list-style-type: none"> 2 EC-130Q & 2 L-382G (av. TOW=135,000 lbs, MTOW=155,000 lbs for EC-130Q) Total of 1,354 flights - 882 FH - 1354 flts - 195,000+ NM monitored

Table 6.2 The main sources of information about firefighting aircraft usage and loads.

Document	Requirements
Ref. 2	<ul style="list-style-type: none"> §4.9: If fatigue life limitation has been established it may remain in force for a limited period not to exceed one year, until more appropriate fatigue life limitations have been substantiated and approved → revise F&DT based on FF environment
Ref. 4	<p>Part 4:</p> <ul style="list-style-type: none"> Define and document a specific mission profile for FF Missions unique to FF should have an operational load report based on instrumented aircrafts. The load report must be reviewed by FAA and Wichita State University <p>Part 7: Certification will be based on:</p> <ul style="list-style-type: none"> FAA Type Certificate FAA approved baseline F&DT Analysis FAA approved evaluation of the loads FAA approved maintenance and inspection programs based on FF usage Each aircraft shall be equipped with an Operational Loads Monitoring System (OLM) <p>The evaluation of the airtanker usage is to be performed in two distinct stages. The first stage involves a preliminary evaluation of the airframe based on historical airtanker load histories (...). The second stage involves utilizing actual recorded data to update the initial preliminary evaluation</p> <p>(...) Fatigue and damage tolerance analyses of the baseline fatigue critical structure / PSEs must be re-evaluated utilizing the airtanker fatigue spectra. This evaluation must be performed using fatigue and crack growth analytical methods and include the effects on PSE baseline inspections as well as any structural component life limits established by WFD critical structure. In order to perform a thorough evaluation, fatigue critical structure / PSEs shall be determined by the AC 91-82 fatigue critical structure criteria and with a supportable rational.</p>

Table 6.3 The main requirements specific to the F&DT analysis of FF aircraft.

Specific airworthiness specifications are given in Ref. 2 (AC525-012 of Transport Canada) and Ref. 4 (the Airworthiness Assurance Guide of the USFS). The main requirements specific to the F&DT analysis of FF aircraft are summarised in Table 6.3.

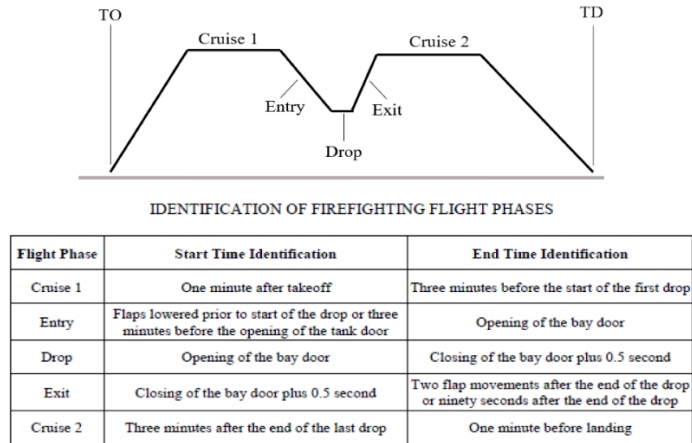


Figure 6.4 Example of a typical firefighting mission profile for the C27J aircraft.

The main focus of the activity is determining specific FF spectra for the aircraft. The typical FF mission is described in the diagram shown in Figure 6.4

Following this definition, FF spectra for both gusts and manoeuvres have been developed and are compared to the standard references defined in ESDU 69023 for gusts and in MIL-A-87221 for manoeuvres of a transport aircraft carrying cargo.

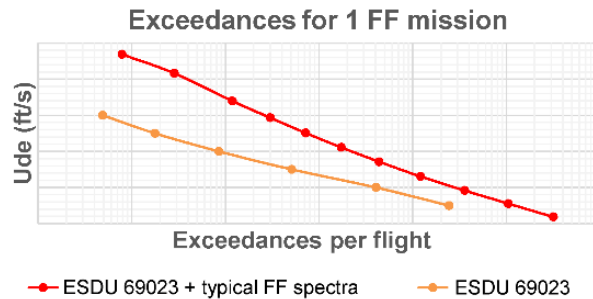


Figure 6.5 Vertical gust spectra: comparison between ESDU 69023 and typical FF spectra.

In Figure 6.5 a comparison is made between the *ESDU 69023* and *typical FF gust spectra* relevant for a phase, taken as an example, of the FF mission of the C27J aircraft. Analyses showed that, as for the specific case shown, the gust spectra for FF mission are more severe than the standard ones for all the phases of the mission.

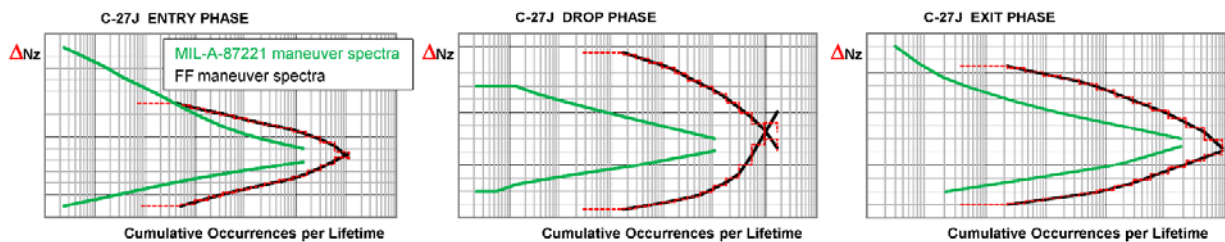


Figure 6.6 MIL-A-87221 manoeuvre spectra compared to the FF ones for the C27J

In Figure 6.6 a comparison is made between the MIL-A-87221 manoeuvre spectra (CTransport, cargo class, training) and the typical FF manoeuvre spectra.

As can be seen from the plots in Figure 6.6 the manoeuvre spectra for FF missions are more severe than the standard ones.

For the C-27J, a preliminary evaluation of the mission mixing with the FF role has been carried out using the typical FF spectra. This evaluation of the C-27J suggests that:

- Operational phases (entry, drop and exit) account for the majority of mission damage. The drop phase is the most severe.
- Gust spectra show higher occurrences (in excess of one order of magnitude) at high gust velocities than in ESDU 69023.
- The manoeuvre spectrum shows a higher occurrence (more than two orders of magnitude) than that predicted by MIL-A-87221 cargo transport training missions.
- The manoeuvre spectrum must be considered in the evaluation of GAG damage due to its significant contribution.
- One FF mission (15–20 minutes per mission) with one drop generates approximately the same fatigue damage as three basic logistic missions (two and a half hours per mission).

6.3 TORNADO: Technical Evaluation-Fatigue and DT Analysis (Leonardo Aircraft Division)

Following several failures involving the upper and lower pivot bushings of the diffusion joint on Tornado aircraft (see Figure 6.7), a technical assessment was conducted, including fatigue and DT analysis.

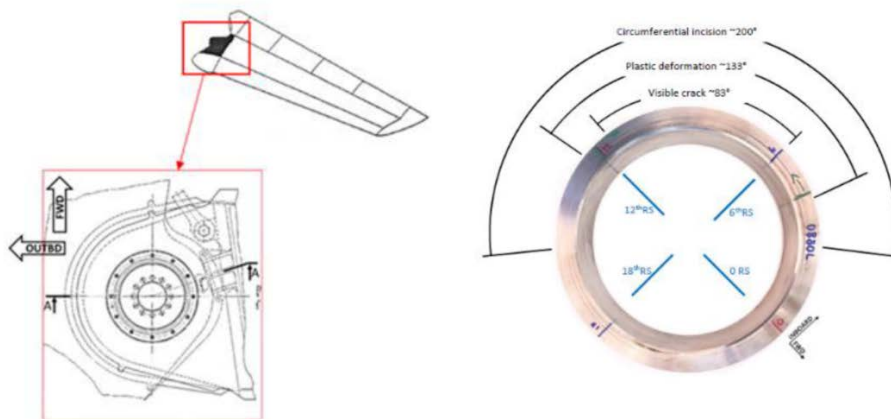


Figure 6.7 Tornado lower pivot bushings of the diffusion joint

These failures occur when the required gap between the bushing and the corresponding bearing, maintained by a Teflon liner, becomes worn. Strength studies have confirmed that, once the required gap is reduced and the bushing comes into contact with the inner sleeve of the bearing, the contact stress becomes significant enough to cause the bushing to break when the imposed displacement exceeds the residual safe margin of -0.06 mm. This is due to a local stress that reaches the ultimate strength of the material. Consequently, rupture occurs almost immediately and there is no evidence of crack propagation due to fatigue.

Leonardo laboratories have conducted several tests on the part, namely: Visual/stereomicroscope examination; NDI evaluation; macroscopic inspection; hardness test; chemical, metallographic and fractographic analyses.

Visual checks showed evident signs of contact on the external surface. The NDI, performed using dye penetrant inspection, revealed a crack extending 215 mm (rather than 175 mm as indicated by the visual check) and deformation of the contact surface. The hardness test and chemical and metallographic analysis showed that the part was manufactured in accordance with the specifications, with no signs of metallurgical defects.

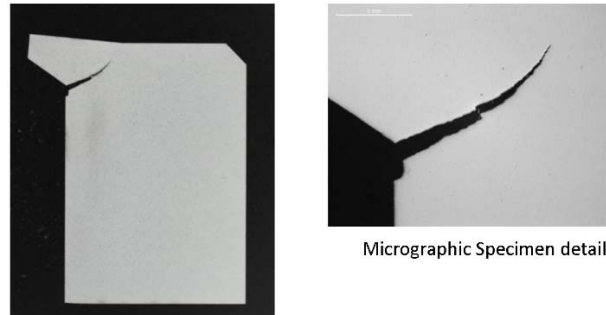


Figure 6.8 Pivot bushings micrographic specimen

Micrographic analysis (see Figure 6.8 and Figure 6.9) shows a non-passing-through crack that starts from the groove at the corner between the bushing's contact surface and its shoulder, and propagates towards the lower surface of the bushing. The crack starts (see Figure 6.9) in the groove and extends to the point at which the lower bushing surface comes into contact with the inner sleeve (indicating an incision). Micrographic analysis of the bushing crack reveals mixed propagation modes: intergranular and transgranular.

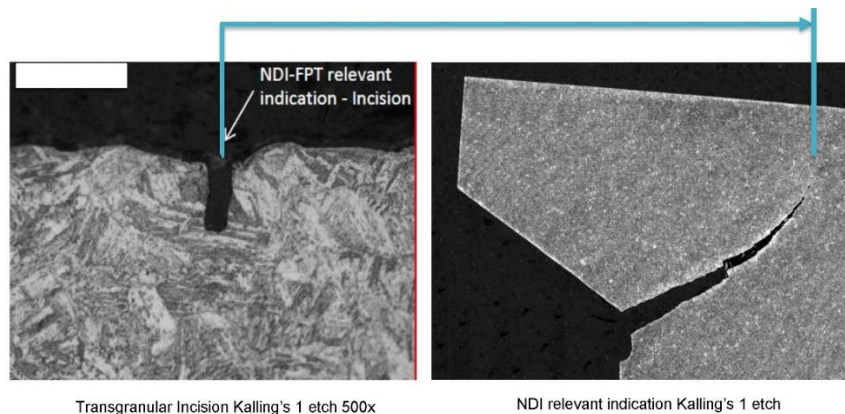


Figure 6.9 Pivot bushings micrographic analysis results

Examination of the fractographic specimen confirmed that the crack originates from multiple initiation points located at the bushing groove and advances via step propagation. The entire fracture surface appears to be affected by a mixed brittle rupture mechanism (intergranular and transgranular), with traces of fatigue. The brittle transgranular fracture, instead, cutting through the grains, forms cleavage planes; the cleavage initiation is located on the edge of the previous grain.

A third rupture mechanism present on the failure surface shows few signs of fatigue striation and minor interline fatigue.

As the Tornado aircraft was designed as a 'Safe Life' jet, the Damage Tolerance approach cannot be used to provide clearance based on the results of structural inspections via NDI. In this case, a study was conducted to provide the Italian Air Force with sufficient information to mitigate the risk of flying with a cracked bushing.

The analysis showed that, given the known defects in the bushes, it was possible to demonstrate that the critical crack size would not be reached between two consecutive gap checks, provided that

the maximum stress in the spectrum remained equal to or below a given value. The latter was calculated based on the load severity index of the Italian Tornado fleet, which has accumulated more than 3,000 flight hours (FH).

However, the analyses are based on strong assumptions, as there is no known means of controlling the real applied loads. Furthermore, the relationship between Teflon wear, gap reduction and contact stress has not been determined. The material fracture mechanics characteristics come from the NASGRO database, but should be determined by means of a dedicated test campaign.

6.4 EUROFIGHTER Production Major Airframe Fatigue Test (Leonardo Aircraft Division)

The PMAFT was a full-scale test that aimed to demonstrate the airframe's durability by achieving a fatigue life of 18,000 hours, enabling a 6,000 hours fatigue life clearance to be issued for the Eurofighter aircraft. The test items were loaded to reproduce the manoeuvres defined in the Composite Set of Training Missions (CSTMs). The fatigue test, which was performed in Brough, UK, was completed in 2018.

As the Leonardo Aircraft Division is responsible for the design of the wings, the Fatigue Office in Turin was tasked with justifying all the damage that occurred to the left wing (see Table 6.4 for the detailed list). During the period covered by this National Review, the Fatigue Office has continued its work on explaining the wing fatigue damage that occurred between 15,000 and 18,000 test hours.

SFH	Part	Damage Description	Representative
15000	Rear Fuselage Upper Panels XXXXX	Delamination occurred in different ten new locations	yes
15000	RH Tip Pod - OB Front Spar Attachment Lug	Attachment lug bush XXXXXXXXXXXX had migrated forward	yes
17209	RH Wing Rib XXXXX Machined Part	ITSPL right I/B Pylon Housing that have been found cracked	TBD (pending results of Tear Down Analysis)
18000	LH Wing Rib XXXXX Machined Part	ITSPL left I/B Pylon Housing that have been found cracked	TBD (pending results of Tear Down Analysis)
18000	Rear Fuselage Panel XXXXX	One of the attachment bolt grommets had become detached from the panel XXXXX (LHS)	no
18000	LH Wing Fixed Leading Edge Landing	Cracks were found in the LHS fixed leading edge assembly on the lower wing skin closing plate panel landing XXXXXXXX	no
18000	RH Wing Fixed Leading Edge Landing	Cracks were found in the RHS fixed leading edge assembly on the lower wing skin closing plate panel landing XXXXXXXX	no
18000	RH Wing Removable Panel XXXXXXXX	Panel (XXXXXXXXXX) was mechanically damaged by the inboard R/H side slat track lug	no
18000	LH RH Wing Rib XXXXX Machined Part (OB stud housing)	LH Outboard stud housing was found to have crack like indications at 3 locations	TBD (pending results of Tear Down Analysis)

Table 6.4 EFA fatigue test damages on the wings occurred between 15000 and 18000 Test Hours.

6.5 M345 Fatigue test on component status (Leonardo Aircraft Division)

The M-346 and M-345 are trainer aircraft developed by the Leonardo Aircraft Division. The former is an advanced combat pilot trainer, while the latter is a low-cost aircraft designed for basic and advanced training.



Figure 6.10 Leonardo M-345 trainer

The M-345 (see Figure 6.10) is a jet aircraft equipped with modern avionics, characterised by operating costs comparable to those of a high-powered turboprop trainer. Based on experience in the M-346 programme, the M-345's avionics include a state-of-the-art human-machine interface, and the Embedded Tactical Training System (ETTS) enables highly complex tactical scenarios to be reproduced during training flights.

The M345 shares the same certification basis as the M346: a durability approach with a scatter factor of 2, applied to the life demonstrated by means of a full-scale fatigue test. Fatigue tests on major components have been completed, as shown in Table 6.5.

M 345 trainer A/C	
Item	Completion
Wing	26 %
Fuselage + Vertical tail	20 %
Hor. Tail + Equilibrator	100 %
Rudder	100%
Ailerons	100%
Flight Control	initial phase

Table 6.5 Trainer aircrafts Fatigue Tests status.

6.6 GCAP–Global Combat Air Programme (Leonardo Aircraft Division)

The Global Combat Air Programme (GCAP) is a multinational collaborative project involving Italy, the United Kingdom, and Japan. Leonardo is a strategic GCAP partner, alongside BAE Systems in the UK and Mitsubishi Heavy Industries in Japan. The programme's shared ambition is to produce a next-generation fighter aircraft by 2035. This aircraft will form the 'core platform' of a 'system of systems' operating across the air, land, sea, space and cyber domains, connecting crewed and uncrewed peripheral systems.

The Leonardo Aircraft Division Fatigue Office is contributing to the following aspects:

- Defining the fatigue approach for the sixth-generation aircraft, thereby establishing the underlying requirements.
- performing studies to define a G-spectrum based on substantial legacy company data from fleet management
- performing studies to define solutions for reducing the aircraft's weight.
- developing a Leonardo proposal for the sixth-generation SHM system;
- researching new sensors and materials for the sixth-generation SHM system.

7 REFERENCES

- [1] Carlos G. Dávila et al. (2020), Evaluation of Fatigue Damage Accumulation Functions for Delamination Initiation and Propagation, NASA/TP-2020-220584
- [2] P. Ballarin et al. (2025), Fatigue Propagation of Interface Damages in Layered Composites, 32nd ICAF Symposium – Xi'an, 09-12 June 2025